

1 **Examination of effects of aerosols on a pyroCb and their dependence on fire**
2 **intensity and aerosol perturbation**

3

4

5 Seoung Soo Lee¹, George Kablick III^{2,3}, Zhanqing Li², Chang-Hoon Jung⁴, Yong-Sang
6 Choi⁵, Junshik Um⁶, Won Jun Choi⁷

7

8 ¹Research Foundation, San Jose State University, San Jose, California, USA

9 ²Earth System Science Interdisciplinary Center, University of Maryland, College Park,
10 Maryland, USA

11 ³US Naval Research Laboratory, Washington, DC, USA

12 ⁴Department of Health Management, Kyungin Women's University, Incheon, South
13 Korea

14 ⁵Department of Environmental Science and Engineering, Ewha Womans University,
15 Seoul, South Korea

16 ⁶Department of Atmospheric Sciences, Division of Earth Environmental System, Pusan
17 National University, Busan, South Korea

18 ⁷National Institute of Environmental Research, Incheon, South Korea

19

20

21

22

23

24

25 Abstract

26

27 Through a modeling framework, this study investigates how a pyrocumulonimbus (pyroCb)
28 event influences water vapor concentrations and cirrus cloud properties near the tropopause,
29 specifically focusing on how fire-produced aerosols affect this role. Results from a case
30 study show that when observed fire intensity is high, there is an insignificant impact of
31 fire-produced aerosols on the development of the pyroCb and associated changes in water
32 vapor and cirrus clouds near the tropopause. However, as fire intensity weakens, effects
33 of those aerosols on microphysical variables and processes such as droplet size and
34 autoconversion increase. Due to this, aerosol-induced invigoration of convection is
35 significant for pyroCb with weak-intensity fires and associated weak surface heat fluxes.
36 This leads to a situation where there is a greater aerosol effect on the transport of water
37 vapor to the upper troposphere and the production of cirrus clouds with weak-intensity fires,
38 whereas this effect is muted with strong-intensity fires.

39

40

41

42

43

44

45

46

47

48

49

50

51

52

53

54

55

1. Introduction

Recent studies (e.g., Pumphrey et al., 2011; Kablick et al., 2018) showed that pyrocumulonimbus (pyroCbs) may transport significant amounts of water vapor to the upper troposphere and the lower stratosphere (UTLS) and can possibly have an impact on seasonal UTLS water vapor budgets. Any change in water vapor in the UTLS has an exceptionally strong influence on the global radiation budget and thus Earth's climate (Solomon et al., 2010). PyroCbs develop cirrus clouds associated with overshooting convective tops that reach the UTLS. Changes in cirrus clouds in the UTLS are known to have a strong influence on the global radiation budget (Solomon et al., 2010). The level of our understanding of impacts of pyroCbs on water vapor and cirrus clouds in the UTLS on a global scale is very low and studies have been conducted to improve this understanding (Fromm et al., 2010). However, this paper does not focus on these pyroCb impacts at the global scale. Instead, this paper aims to gain a process-level understanding of mechanisms that control local impacts of individual pyroCbs on water vapor and cirrus clouds in the UTLS. The examination of these mechanisms can provide useful information to parameterize interactions among pyroCbs, water vapor and cirrus clouds in climate models.

PyroCbs initiate over a fire, and the large surface energy release mainly through fire-induced latent- and sensible-heat fluxes at and near the surface affects the dynamic, thermodynamic and microphysical development of pyroCbs (Fromm et al., 2010; Peterson et al., 2017). However, questions remain about what role the large concentration of cloud condensation nuclei (CCN) contained in smoke has on the vertical development and microphysical properties of pyroCbs. Studies (e.g., Koren et al., 2008; Rosenfeld et al., 2008; Storer et al., 2010; Tao et al., 2012) showed that aerosols affected cumulonimbus clouds, thus raising the possibility that fire-generated aerosols may affect pyroCb development. As an example of aerosol impacts on cumulonimbus clouds, these studies have demonstrated that increases in aerosol loading can decrease the size of droplets (i.e., cloud-liquid particles). Individual aerosol particles act as seeds for the formation of droplets, so increasing aerosol loading leads to more droplets formed. More droplets mean more competition among them for available water vapor needed for their condensational growth, decreasing the size of individual droplets (Twomey, 1977; Albrecht, 1989).

87 Aerosol-induced smaller droplet sizes reduce the efficiency of the growth of cloud-liquid
88 particles to raindrops via autoconversion, a collection process among cloud-liquid particles
89 in which they become raindrops (Pruppacher and Klett, 1978; Rogers and Yau, 1991). This
90 reduced efficiency leads to less cloud liquid converted to rain and thus more cloud liquid
91 available for transport by updrafts to altitudes above the freezing level. This eventually
92 induces more freezing of cloud liquid, enhanced parcel buoyancy and the invigoration of
93 updrafts and associated convection (Rosenfeld, 2008).

94 The role of fire-generated aerosols in the development of pyroCbs and their effects
95 on water vapor and cirrus clouds in the UTLS lacks a firm scientific understanding, and
96 hence this paper focuses on that role of those aerosols. To examine the role, this study
97 extends the previous modeling work by Kablick et al. (2018). The modeling work therein
98 showed that the effects of fire-generated aerosols on the development of a specific pyroCb
99 and its impacts on the UTLS water vapor and cirrus clouds were negligible compared to
100 the effects of fire-generated heat fluxes. However, aerosol effects on cloud development
101 vary with cloud properties such as typical updraft speeds (e.g., Khain et al., 2008; Lee et
102 al., 2008; Tao et al., 2012). For simplicity herein, an “updraft” refers to the general upward
103 motion of convective air, or to the actual updraft speed representing the updraft or
104 convective intensity, depending on the context. Typical updrafts are determined by
105 environmental instability as represented by convective available potential energy (CAPE).
106 Lee et al. (2008) demonstrated that different clouds with different typical updrafts showed
107 different sensitivity of cloud microphysical and thermodynamic development to aerosol
108 concentration. Hence, it is hypothesized that aerosol effects on pyroCb development and
109 its impacts on the UTLS water vapor and cirrus clouds vary depending on the pyroCb
110 typical updrafts.

111 To examine the potential variation of aerosol effects on pyroCb development and its
112 impacts on the UTLS water vapor and cirrus clouds with typical updrafts of pyroCbs,
113 numerical simulations are performed. Simulated is the pyroCb case examined by Kablick
114 et al. (2018) using a cloud-system resolving model (CSRM). The CSRM is capable of
115 resolving cloud-scale dynamic and thermodynamic processes. The basic modeling
116 methodology in this study is similar to that used by Kablick et al. (2018). However, this

117 study uses a more sophisticated microphysical scheme, i.e., a bin scheme, rather than the
118 two-moment bulk scheme used by Kablick et al. (2018).

119 Note that Kablick et al. (2018) examined aerosol effects on the convective
120 development of a specific pyroCb case with a typical updraft framework. The present study
121 expands upon that work by performing sensitivity simulations in which typical updrafts in
122 the pyroCb vary, enabling us to ascertain the dependence of aerosol effects on typical
123 updrafts. Note that CAPE, which determines typical updrafts in convective clouds, is
124 strongly dependent on surface latent and sensible heat fluxes (e.g., Houze, 1993), and in
125 the case of pyroCbs, these fluxes are strongly controlled by fire intensity. Therefore, the
126 present sensitivity simulations enable us to study the dependence of those aerosol effects
127 on fire intensity. Since fire intensity is the dominant driver of the pyroCb typical updrafts,
128 these typical updrafts are henceforth referred to as fire-driven updrafts.

129 Effects of fire-induced increases in aerosol concentration on pyroCbs are likely
130 dependent on how much aerosol concentration increases (aerosol perturbation) (e.g.,
131 Rosenfeld et al., 2008; Koren et al., 2012). This study examines this dependence, not
132 studied by Kablick et al. (2018).

133

134 **2. Modeling framework**

135

136 We use the Advanced Research Weather Research and Forecasting (ARW) model, a
137 nonhydrostatic compressible model, as the CSRM. Prognostic microphysical variables are
138 transported with a fifth-order monotonic advection scheme (Wang et al., 2009). Shortwave
139 and longwave radiation is parameterized by the Rapid Radiation Transfer Model (RRTM;
140 Mlawer et al., 1997; Fouquart and Bonnel, 1980).

141 To represent microphysical processes, the CSRM adopts a bin scheme based on the
142 Hebrew University Cloud Model described by Khain et al. (2009). The bin scheme solves
143 a system of kinetic equations for the size distribution functions of water drops, ice crystals
144 (plate, columnar and branch types), snow aggregates, graupel and hail, as well as cloud
145 condensation nuclei (CCN) and ice nuclei (IN). Each size distribution is represented by 33
146 mass doubling bins, i.e., the mass of a particle m_k in the k th bin is determined as $m_k =$
147 $2m_{k-1}$.

148 A cloud-droplet nucleation parameterization based on Köhler theory represents cloud-
149 droplet nucleation. Arbitrary aerosol mixing states and aerosol size distributions can be fed
150 to this parameterization. To represent heterogeneous ice-crystal nucleation, the
151 parameterizations by Lohmann and Diehl (2006) and Möhler et al. (2006) are used. In these
152 parameterizations, contact, immersion, condensation-freezing, and deposition nucleation
153 paths are all considered by taking into account the size distribution of IN, temperature and
154 supersaturation. Homogeneous aerosol (or haze particle) and droplet freezing is also
155 considered following the theory developed by Koop et al. (2000).

156

157 **3. Case description and simulations**

158

159 **3.1 Control run**

160

161 The control run for an observed pyroCb case involved a forested site in the Canadian
162 Northwest Territories (60.03° N, 115.45° W). Kablick et al. (2018) give details about the
163 site and pyroCb case. The control run is identical to the Full Simulation in Kablick et al.
164 (2018) except for the different microphysical schemes. The period covered by the control
165 run is from 12:00 GMT on August 5th to 12:00 GMT on August 6th in 2014 and captures
166 the initial, mature, and decaying stages of the pyroCb. As described by Kablick et al. (2018),
167 balloon soundings of winds, temperature and dew-point temperature were obtained every
168 6 hours from the Ft. Smith observation station near the forested site. Sounding data at 12:00
169 GMT on August 5th prescribe the initial atmospheric conditions. Temperature and humidity
170 tendencies at each altitude from sequential soundings are obtained and applied to the
171 control run every time step by interpolation in a horizontally homogeneous manner. These
172 tendencies represent the impacts of synoptic- or large-scale motion on temperature and
173 humidity (Grabowski et al., 1996; Krueger et al., 1999; and Lee et al., 2018). The control
174 run is performed in a three dimensional domain with horizontal and vertical extends of 300
175 km and 20 km, respectively. The simulation horizontal and vertical resolutions are 500 m
176 and 200 m, respectively, to resolve cloud dynamic and thermodynamic processes.

177 Figure 1 shows a satellite image of the observed pyroCb and the fire spot (spatial length
178 is ~40 km) when the cloud is about to advance into its mature stage. To emulate this in the

179 simulation, a fire spot with a diameter of 40 km is placed at the center of the simulation
180 domain (Figure 2). In the fire spot, the surface latent and sensible heat fluxes are set at
181 1800 and 15000 W m⁻², respectively. In areas outside of the fire spot, the surface latent and
182 sensible heat fluxes are set at 310 and 150 W m⁻², respectively. These surface heat-flux
183 values follow previous studies which adopt boreal forest emissions (Trentmann et al., 2006;
184 Luderer et al., 2006). Following Kablick et al. (2018), the surface heat-flux values are
185 prescribed with no temporal variation and no consideration of interactions between heat
186 fluxes and the atmosphere in the control run. Thus, the setup for the surface heat fluxes is
187 idealized, enabling a better isolation of aerosol effects on pyroCb development and its
188 impacts on the UTLS water vapor and cirrus clouds by excluding effects of interactions
189 between the surface heat fluxes and atmosphere on this development and its impacts.

190 For the selected pyroCb case, aerosol chemical composition, size distribution and
191 concentration are unknown. Hence, in (outside) the fire spot at the first time step, the
192 concentration of aerosols acting as CCN is prescribed to be 15000 (150) cm⁻³. This
193 prescription is for the planetary boundary layer (PBL) and the concentration decreases
194 exponentially with height above the PBL top. These prescribed aerosol concentrations are
195 typically observed in fire spots and their background (Pruppacher and Klett, 1997; Seinfeld
196 and Pandis, 1998; Reid et al., 1999; Andreae et al., 2004; Reid et al., 2005; Luderer et al.,
197 2009).

198 Reid et al. (2005) showed that aerosol mass produced by forest fires was generally
199 composed of (by mass) ~50-70% organic-carbon (OC) compounds, ~5-10% black-carbon
200 (BC) material, and ~20-45% inorganic species. The approximate median value of each of
201 these chemical component percentage ranges determines the aerosol particle composition
202 in the control run, i.e., 60% OC, 8% BC, and 32% inorganic species. OC is assumed to be
203 water soluble and composed of 18 % levoglucosan (C₆H₁₀O₅, density = 1600 kg m⁻³, van't
204 Hoff factor = 1), 41 % succinic acid (C₄H₆O₄, density = 1572 kg m⁻³, van't Hoff factor =
205 3), and 41 % fulvic acid (C₃₃H₃₂O₁₉, density = 1500 kg m⁻³, van't Hoff factor = 5) based
206 on typically observed chemical composition of OC compounds over fire sites (Reid et al.,
207 2005). In the control run, the inorganic species are assumed to be ammonium sulfate, a
208 representative inorganic species associated with fires (Reid et al., 2005). This chemical

209 composition taken for aerosol particles is assumed to be spatiotemporally unvarying in the
210 control run.

211 The control run adopts the unimodal lognormal distribution as an initial aerosol size
212 distribution, a reasonable assumption in fire sites (Reid et al., 2005; Knobelspiessel et al.,
213 2011; Lee et al., 2014). Those studies reported that in general, median and standard
214 deviation aerosol diameters range from $\sim 0.01 \mu\text{m}$ to $\sim 0.03 \mu\text{m}$ and from $\sim 2.0 \mu\text{m}$ to ~ 2.2
215 μm , respectively, for aerosols as CCN. The approximate median values of these ranges
216 determine median and standard deviation diameters of aerosols as CCN in the control run,
217 i.e., $0.02 \mu\text{m}$ and $2.1 \mu\text{m}$, respectively. Assumed identical in the control run are IN and
218 CCN aerosol properties except that at the first time step, (1) their median and standard
219 deviation aerosol diameters differ, and (2) the IN concentration is 100 times lower than the
220 CCN concentration (Pruppacher and Klett, 1978; Fan et al., 2014 and 2017). Following
221 Seinfeld and Pandis (2006) and Phillips et al. (2007), for aerosols as IN, median and
222 standard deviation aerosol diameters are assumed to be $0.1 \mu\text{m}$ and $1.6 \mu\text{m}$, respectively,
223 which are typical values in the continent.

224 Airflow in clouds diffuses and advects aerosols. After activation or capture by
225 precipitating hydrometeors, aerosols are transported within hydrometeors and removed
226 from the atmosphere once these hydrometeors reach the surface. Once clouds disappear
227 completely at any grid point, aerosol size distribution and number concentration recover to
228 the background values at the first time step. This assumption simulates overall aerosol
229 properties and their impacts on clouds and precipitation reasonably well (Morrison and
230 Grabowski, 2011; Lebo and Morrison, 2014; Lee et al., 2016). This assumption means that
231 fire continuously produces aerosols to maintain the initial background aerosol
232 concentration.

233 Located to the northeast of the fire spot is the observed cirrus cloud at the top of the
234 pyroCb, since winds advect the cloud northeastward (Figure 1). The extent of the observed
235 cirrus cloud is $\sim 100 \text{ km}$. Figure 2 shows the simulated field of cloud-ice mass density at a
236 time that corresponds to the satellite image in Figure 1, representing the simulated cirrus
237 cloud in the control run. Located to the northeast of the fire spot is the simulated cirrus
238 cloud, and the extent of this cloud is $\sim 100 \text{ km}$. The morphologies of the observed and
239 simulated cirrus clouds agree well.

240 The average liquid-water path (LWP) over areas with non-zero LWP in the control run
241 is 960 g m^{-2} , and the average ice-water path (IWP) over areas with non-zero IWP in the
242 control run is 202 g m^{-2} . These simulated LWP and IWP are $\sim 10\%$ different from the
243 satellite-retrieved values. In this study, droplet mass but not raindrop mass is used to obtain
244 liquid-water content (LWC) and LWP, and the mass of ice crystals but not the mass of
245 snow aggregates, graupel and hail is used to obtain ice-water content (IWC) and IWP.
246 Drops with radii smaller (greater) than $20 \mu\text{m}$ are classified as droplets (raindrops). The
247 average cloud-top and cloud-base heights over the life span of the pyroCb are 10.3 km and
248 3.6 km in the control run, respectively, and these simulated heights are $\sim 7\%$ different from
249 the satellite-retrieved values. Overall, cloud macro-physical structures, as represented by
250 LWP, IWP, cloud-top and cloud-base heights, are simulated reasonably well compared to
251 the observation.

252 Compared are the control-run and observed reflectivity fields. Kablick et al. (2018)
253 provide details about the reflectivity field observed by CloudSat. Observations and the
254 control run both show increasing reflectivity up to $\sim 7 \text{ km}$, decreasing reflectivity between
255 $\sim 7 \text{ km}$ and $\sim 11 \text{ km}$ and insignificant changes in reflectivity above $\sim 11 \text{ km}$ in altitude
256 (Figure 3). The average reflectivity over altitudes along the Cloudsat path in the control
257 run is -8.1 dBZe , $\sim 15\%$ different from the observed value. Hence, the reflectivity field is
258 simulated fairly well compared to the observation. These favorable comparisons between
259 the observed and simulated cirrus clouds, cloud macro-physical and reflectivity fields
260 demonstrate that the pyroCb-case simulation reasonably reproduces the event.

261

262 **3.2 Low-aerosol run**

263

264 To see the role played by fire-generated aerosols in the development of the pyroCb and its
265 effects on the UTLS water vapor and cirrus clouds, we repeat the control run by reducing
266 aerosol concentration in the fire spot from 15000 cm^{-3} to the background aerosol
267 concentration (i.e., 150 cm^{-3}). This reduction removes fire-generated aerosols in the fire
268 spot. Hence, comparisons between the control run and this repeated run, referred to as the
269 low-aerosol run, will identify the role played by fire-generated aerosols. The low-aerosol

270 run is identical to the Low Aerosol Simulation in Kablick et al. (2018) except for the
271 different microphysical schemes between them.

272

273 **3.3 Additional runs**

274

275 For the examination of the potential variation of effects of fire-generated aerosols on
276 pyroCb development and its impacts on the UTLS water vapor and cirrus clouds with fire
277 intensity and associated fire-driven updrafts, we repeat the control run by varying fire
278 intensity. Remember that fire intensity controls surface latent and sensible heat fluxes on
279 which fire-driven updrafts are strongly dependent. Therefore, variations in fire-induced
280 surface latent and sensible heat fluxes can represent variations in fire intensity. As a first
281 step, the control run is repeated by reducing fire-induced surface latent and sensible heat
282 fluxes by factors of 2 and 4, respectively. The first repeated run represents a case with
283 medium fire intensity, referred to as “the medium run”. The second repeated run represents
284 a case with weak fire intensity, referred to as “the weak run”. Relative to these repeated
285 runs, the control run represents a case with strong fire intensity. Then, to see effects of fire-
286 generated aerosols on pyroCb development for each of those different fire intensities, the
287 medium and weak runs are repeated with the identical initial aerosol concentration to that
288 in the low-aerosol run. The repeated medium and weak runs are referred to as “the medium-
289 low run” and “the weak-low run”, respectively. The control, medium, and weak runs are
290 the polluted-scenario runs, and the low-aerosol, medium-low, and weak-low runs are the
291 clean-scenario runs.

292 Effects of fire-generated aerosols on pyroCb development and its impacts on the UTLS
293 water vapor and cirrus clouds can also depend on the magnitude of fire-induced increases
294 in aerosol concentration in a fire spot. To test this dependence, for each fire intensity, we
295 repeat the polluted-scenario run by increasing and decreasing the magnitude by a factor of
296 2 in the fire spot but not outside of the fire spot. The simulations with the increased
297 magnitude have an aerosol concentration of 30000 cm^{-3} at the first time step over the fire
298 spot in the PBL, referred to as the control-30000, medium-30000, and weak-30000 runs
299 for strong, medium, and weak fire intensities, respectively. The simulations with the
300 decreased magnitude have an aerosol concentration of 7500 cm^{-3} at the first time step over

301 the fire spot in the PBL, referred to as the control-7500, medium-7500, and weak-7500
302 runs for strong, medium, and weak fire intensities, respectively. Motivated by the analysis
303 described in Section 4.3, we additionally repeat the medium and weak runs with aerosol
304 concentrations of 2000 and 1000 cm^{-3} , respectively, at the first time step over the fire spot
305 in the PBL. The repeated medium (weak) run is referred to as the medium-2000 (weak-
306 1000) run. Table 1 summarizes the simulations.

307 The aerosol concentration of 30000 cm^{-3} (7500, 2000 and 1000 cm^{-3}) over the fire spot
308 corresponds to a situation where fire produces a larger (lower) concentration of aerosols
309 than what is typically observed, i.e., 10000 to 20000 cm^{-3} (Reid et al, 1999; Andreae et al,
310 2004; Reid et al, 2005; Luderer et al., 2009).

311

312 **4. Results**

313

314 **4.1 The control and low-aerosol runs**

315

316 The updraft mass flux was averaged over the simulation period between 17:00 GMT on
317 August 5th, approximately when the pyroCb started to form, and 12:00 GMT on August 6th
318 (Figure 4). The updraft mass flux is one of the most indicative variables of the upward air
319 motion and magnitude of convective invigoration. Since the updraft mass flux is updraft
320 speed that is multiplied by air density, and air density at each altitude varies negligibly,
321 differences in updraft mass fluxes are mostly explained by those in updraft speeds among
322 the simulations. Hence, with good confidence, differences in updraft mass fluxes mean
323 those in updraft speeds.

324 The upper troposphere is defined here to be between ~ 9 km in altitude and the
325 tropopause which is ~ 13 km in altitude. The equilibrium level where the buoyancy of a
326 rising air parcel becomes zero above the level of free convection is the tropopause
327 (Emanuel, 1994). The lower stratosphere is defined here to be between the tropopause and
328 an altitude 10 km above the tropopause. The UTLS is thus between ~ 9 km and ~ 23 km in
329 this study. The defined upper troposphere and lower stratosphere occupy around a quarter
330 of the total vertical extent of the troposphere and stratosphere, respectively.

331 Updraft mass fluxes in the control run are only $\sim 3\%$ greater than those in the low-
332 aerosol run (Figure 4 and Table 2). Given the hundredfold difference in aerosol loading
333 over the fire spot between the runs, this 3% difference in updraft fluxes is negligible. The
334 comparison between water-vapor mass density over the cloudy and non-cloudy columns in
335 the control run demonstrates that there is a substantial 5-fold increase in the amount of
336 water vapor in the part of the UTLS at and above the tropopause due to the pyroCb (Figure
337 5 and Table 2). Henceforth, the UTLS water vapor means water vapor in the part of the
338 UTLS at and above the tropopause.

339 For the simulation period between 17:00 GMT on August 5th and 12:00 GMT on
340 August 6th, the average water-vapor mass fluxes at the tropopause over cloudy and non-
341 cloudy grid columns are 8.30×10^{-6} and 0.57×10^{-6} $\text{kg m}^{-2} \text{s}^{-1}$, respectively. Due to the
342 presence of the pyroCb and associated updrafts in cloudy grid columns, there are
343 substantial increases in fluxes at the tropopause over cloudy grid columns compared to
344 fluxes in the background over non-cloudy grid columns. This explains the larger amount
345 of the UTLS water vapor over the pyroCb than in the background in the control run. The
346 vertical extent of water vapor reaches further up to ~ 16 km by the pyroCb beyond ~ 14 km
347 in the background (Figure 5). This means that air parcels that include water vapor overshoot
348 the tropopause by ~ 3 km in the pyroCb, while those parcels in the background do so by \sim
349 1 km. This implies that air parcels and associated updrafts in the pyroCb are stronger,
350 reaching higher altitudes. Those stronger air parcels enable water-vapor layers to be
351 deepened in the lower stratosphere. These deepened layers and their greater water-vapor
352 mass contribute to more interception of longwave radiation by water vapor in the UTLS
353 over the pyroCb.

354 Similar to the situation with updraft mass fluxes, there is only a small ($\sim 2\%$) increase
355 in the average mass of the UTLS water vapor in the control run versus the low-aerosol run
356 for strong fire intensity (Figure 5 and Table 2). The small variation in updraft mass fluxes
357 between the runs results in a small variation in the average water-vapor fluxes at the
358 tropopause from 8.30×10^{-6} $\text{kg m}^{-2} \text{s}^{-1}$ in the control run to 8.21×10^{-6} $\text{kg m}^{-2} \text{s}^{-1}$ in the low-
359 aerosol run over cloudy columns for the simulation period between 17:00 GMT on August
360 5th and 12:00 GMT on August 6th.

361 The altitude of homogeneous freezing is 9 km, so cirrus clouds composed of ice crystals
362 (or cloud ice) are between 9 km and 13 km in the control run (Figure 6). The amount of
363 cirrus clouds in the control run, represented by the average cloud-ice mass density, ranges
364 from 0.028 to 0.037 g m⁻³ between 9 km and 13 km (Figure 6). The average cloud-ice
365 number concentration and size, represented by ice-crystal volume mean radius, between 9
366 km and 13 km range from 6 to 20 cm⁻³, and from 10 to 20 μm, respectively. Henceforth,
367 “the UTLS cirrus clouds” refer to clouds in the upper troposphere.

368 Updrafts produce supersaturation, which leads to the primary source of cloud-ice mass
369 and associated cirrus clouds via deposition. Due to the negligible variation of updraft mass
370 fluxes, there are negligible variations of supersaturation and deposition (Figure 7). So, there
371 is only a negligible increase (~4%) in UTLS cirrus cloud mass in the control run compared
372 to that in the low-aerosol run (Figure 6 and Table 2). However, mainly due to the larger
373 aerosol concentrations, and associated greater homogeneous aerosol and droplet freezing,
374 there is a significant ~20-fold increase in cloud-ice number concentration and associated
375 with this, there is a significant ~2-fold decrease in cloud-ice size in the control run between
376 9 km and 13 km.

377 In summary, the pyroCb and associated updrafts cause a substantial enhancement of
378 the transport of water vapor to the UTLS at and above the tropopause. Wang (2019) also
379 reported this enhancement. Using modeling work and satellite observation, Wang (2019)
380 indicated that the upward transport of water vapor in deep convective storms was possibly
381 a major pathway through which water substance entered the stratosphere. Wang (2019)
382 showed that the upward transport of water vapor was aided by gravity wave and its
383 breaking in overshooting convective parcels. The pyroCb and its updrafts also produce
384 cirrus clouds. The effects of fire-generated aerosols on the pyroCb updrafts, cirrus cloud
385 mass and the enhancement of the water vapor transport are insignificant when fire intensity
386 is strong.

387

388 **4.2 Dependence of aerosol effects on fire intensity**

389

390 When fire-generated surface heat fluxes and fire intensity increase, in-cloud latent heat is
391 also likely to increase because a major source of in-cloud latent heating is surface heat flux.

392 Therefore, aerosol-induced perturbations of latent heating may be relatively small
 393 compared with large in-cloud latent heat contributed by surface fluxes with very intense
 394 burning. Thus, aerosol-induced increases in parcel buoyancy, updrafts and their impacts on
 395 water vapor and the amount of cirrus clouds are relatively small compared with the large
 396 buoyancy, strong fire-driven updrafts produced by strong fire intensity and their associated
 397 impacts on water vapor and the amount of cirrus clouds.

398 When fire intensity and fire-generated surface heat fluxes decrease, in-cloud latent heat
 399 is also likely to be smaller. Here, we are interested in how the magnitude of an aerosol-
 400 induced perturbation of latent heating for a pyroCb with weak fire intensity compares to
 401 that with strong fire intensity. This is to evaluate the possibility that with background in-
 402 cloud latent heat varying with fire intensity, the relative magnitudes of aerosol-induced
 403 perturbations of latent heat and surface flux-dominated latent heat may vary.

404

405 **4.2.1 Effects of Updrafts on the UTLS water vapor and cirrus clouds**

406

407 The average updraft mass fluxes in the low-aerosol, medium-low and weak-low runs
 408 represent fire-driven updrafts for strong, medium and weak fire intensities, respectively
 409 (Figure 4). Due to different fire intensity and associated CAPE, fire-driven updrafts vary
 410 between these runs. All weak, medium and strong fire intensity cases show aerosol-induced
 411 increases in updraft mass fluxes (Figure 4 and Table 2). Of interest is that the greatest
 412 percentage increase in updraft mass flux is in the case of weak fire (weak-low to weak
 413 runs), smallest in the case of strong fire (low-aerosol to control runs), and intermediate in
 414 the case of medium fire (medium-low to medium runs) (Figure 4 and Table 2). Here, the
 415 percentage difference, including both the percentage increase and decrease, is the relative
 416 difference in the value of variables between the polluted-scenario and clean-scenario runs
 417 for each fire intensity. The following equation determines this percentage difference for
 418 the strong fire intensity case:

419

$$420 \frac{\text{Control run minus low-aerosol run}}{\text{Low-aerosol run}} \times 100 (\%) \quad (1)$$

421

422 Replacing the control run with the medium (weak) run, and the low-aerosol run with the
 423 medium-low (weak-low) run in Equation (1) determines the percentage difference for the
 424 medium (weak) fire intensity case. Associated with the greater increases in updraft mass
 425 fluxes, the percentage increases in the UTLS water vapor and cloud-ice mass (Equation 1)
 426 are greater in the case of weaker fire (Figures 5 and 6 and Table 2).

427 In this section, we see that although fire-produced aerosols invigorate updrafts in all
 428 three types of fire intensity, the invigoration-induced increases in the UTLS water-vapor
 429 and cloud-ice mass increase as fire intensity weakens.

430

431 **4.2.2 Volume mean radius of droplets (R_v)**

432

433 **a. Cloud droplet number concentration (N_d) and LWC**

434

435 The simulation period is divided into four sub-periods for this next analysis: period 1
 436 between 17:00 and 19:00 GMT on August 5th (initial formation of the pyroCb), period 2
 437 between 19:00 and 21:00 GMT on August 5th, and period 3 between 21:00 GMT and 23:00
 438 GMT on August 5th (initial stages of cloud development), and period 4 between 23:00 GMT
 439 on August 5th and 12:00 GMT on August 6th (mature and decaying stages). The average N_d
 440 over period 1 decreases as the fire intensity and updrafts decrease (Figure 8). The polluted-
 441 scenario run has higher aerosol concentrations over the fire spot (Table 1), leading to the
 442 much higher average N_d in the polluted-scenario run than in the clean-scenario run for each
 443 fire intensity. Increasing N_d enhances competition among droplets for a given amount of
 444 water vapor. Enhanced competition eventually curbs the condensational growth and
 445 reduces droplet size (R_v). This explains why the average R_v over period 1 is smaller in the
 446 polluted-scenario run (Figure 8). Of interest is that as fire intensity weakens, although the
 447 average N_d decreases, the average R_v decreases not only among the polluted-scenario runs
 448 but also among the clean-scenario runs over the fire spot (Figure 8). This is because R_v is
 449 proportional to $(\frac{LWC}{N_d})^{\frac{1}{3}}$ based on the following Equation (2):

450

$$451 \quad R_v = \left(\frac{3}{4\pi\rho_w}\right)^{\frac{1}{3}} \left(\frac{LWC}{N_d}\right)^{\frac{1}{3}} \quad (2)$$

452

453 Here, ρ_w represents water density at a constant value of 1000 kg m^{-3} , so $(\frac{3}{4\pi\rho_w})^{\frac{1}{3}}$ has a
 454 constant value. LWC represents the given amount of water available for the condensational
 455 growth of droplets. This proportionality means that for a given N_d , a decrease in LWC
 456 decreases R_v . The average LWC over period 1 also decreases with weakening fire intensity
 457 not only among the polluted-scenario runs but also among the clean-scenario runs (Figure
 458 8). Effects of LWC on R_v outweigh those of N_d , leading to the decrease in the average R_v
 459 with weakening fire intensity (Figure 8).

460 Using the average LWC and N_d from Figure 8, $(\frac{LWC}{N_d})^{\frac{1}{3}}$ decreases by $1.50 \times 10^{-5} \text{ kg}$
 461 from $3.50 \times 10^{-5} \text{ kg}$ in the control run to $2.00 \times 10^{-5} \text{ kg}$ in the weak run, while it decreases by
 462 $9.80 \times 10^{-6} \text{ kg}$ from $1.03 \times 10^{-4} \text{ kg}$ in the low-aerosol run to $9.32 \times 10^{-5} \text{ kg}$ in the weak-low run.
 463 Associated with this, the average R_v shows a 47 % reduction from the control to weak runs,
 464 while it shows a 10 % reduction from the low-aerosol to weak-low runs during period 1
 465 (Figure 8).

466 In summary, the simulated LWC, N_d , their variations with fire intensity, and the
 467 functional relation between LWC, N_d and R_v lead to a situation where R_v decreases much
 468 more among the polluted-scenario runs than among the clean-scenario runs during the
 469 period when the pyroCb initially forms.

470

471 **b. Equilibrium supersaturation**

472

473 During period 1, as fire intensity weakens and updraft speed decreases, parcel equilibrium
 474 supersaturation decreases and thus, the minimum size of activated aerosol particles
 475 increases not only among the clean-scenario runs but also among the polluted-scenario runs.
 476 When the production of parcel supersaturation by updrafts and the consumption of
 477 supersaturation by droplets balance out, parcel supersaturation reaches parcel equilibrium
 478 supersaturation (Rogers and Yau, 1991). Mostly due to greater aerosol concentrations,
 479 associated average equilibrium supersaturation and minimum size of activated aerosol
 480 particles over areas with positive updraft speeds and period 1 are lower and larger,

481 respectively, in the polluted-scenario run than in the clean-scenario run for each fire
482 intensity (Rogers and Yau, 1991).

483 The average equilibrium supersaturation decreases from 0.21% in the control run to
484 0.10% in the weak run. Associated with this, the average minimum diameter increases from
485 0.09 μm in the control run to 0.12 μm in the weak run over period 1. The average
486 equilibrium supersaturation decreases from 0.55% in the low-aerosol run to 0.31% in the
487 weak-low run, and the average minimum size increases from 0.04 μm in the low-aerosol
488 run to 0.07 μm in the weak-low run over period 1.

489 The increase in the minimum-activation size with weakening fire intensity occurs
490 closer to the right tail of the assumed unimodal aerosol size distribution among the
491 polluted-scenario runs than among the clean-scenario runs. A smaller portion of the total
492 aerosol concentration is in the size range closer to the right tail of the distribution as long
493 as the range is on the right-hand side of the distribution peak where most of aerosol
494 activation occurs. So, a similar increase in the average minimum-activation size for a
495 weakened fire results in a smaller percentage reduction in the total activated aerosol
496 concentration and thus N_d among the polluted-scenario runs during period 1. The average
497 N_d over period 1 decreases by 8% from the control to weak runs. The average N_d decreases
498 by 76% from the low-aerosol to weak-low runs (Figure 8). This contributes to a greater
499 reduction in R_v as fire intensity weakens among the polluted-scenario runs during period 1.
500 This is for a similar LWC between the polluted-scenario and clean-scenario runs for each
501 fire intensity (Figure 8).

502 In association with larger aerosol concentration and the assumed aerosol size
503 distribution, a smaller percentage variation of the number of activated aerosols and N_d with
504 fire intensity is simulated in the polluted-scenario runs than in the clean-scenario runs. This
505 smaller variation of N_d aids the greater reduction in R_v among the polluted-scenario runs.

506

507 **4.2.3 Autoconversion, freezing, deposition and condensation**

508

509 Autoconversion is proportional to the size of cloud droplets (Pruppacher and Klett, 1978;
510 Rogers and Yau, 1991; Khairoutdinov and Kogan, 2000; Liu and Daum, 2004; Lee and
511 Baik, 2017). Due to the larger R_v during period 1, the subsequent average autoconversion

512 rates over period 2 are higher in the clean-scenario run than in the polluted-scenario run
513 for each fire intensity (Figure 9a). Due to the larger absolute and percentage reduction in
514 R_v among the polluted-scenario runs than among the clean-scenario runs with weakening
515 fire intensity during period 2, the average autoconversion rates decrease by 74% (14%)
516 from the control (low-aerosol) to weak (weak-low) runs (Figure 9a). Associated with this,
517 differences in the average autoconversion rates between the polluted-scenario and clean-
518 scenario runs increase as fire intensity weakens during period 2 (Figure 9a).

519 The increasing differences in autoconversion rates between the polluted-scenario
520 and clean-scenario runs increase those differences in the amount of cloud liquid available
521 for freezing with weakening fire intensity (Figure 9a). Thus, differences in the average rate
522 of cloud-liquid freezing and freezing-related latent heat over the period 2 between the runs
523 increase with weakening fire intensity (Figure 9a). Enhanced freezing-related latent heat
524 strengthens updrafts in places where freezing occurs and this, in turn, enhances deposition
525 and deposition-related latent heat (Lee et al., 2017). Although the average deposition over
526 period 2 is slightly lower, those strengthened updrafts enable the average deposition and
527 deposition-related latent heat to be greater in the polluted-scenario run than in the clean-
528 scenario run for each fire intensity during period 3 (Figures 9a and 9b). Differences in the
529 average freezing rate (and thus the average freezing-related latent heating) between the
530 runs do not change much up to ~20:30 GMT (Figure 10). However, after ~20:30 GMT,
531 these differences start to increase as time goes by for each fire intensity. This is because as
532 convection intensifies, the transport of cloud liquid to places above the freezing level starts
533 to be effective around 20:30 GMT. The greater freezing and thus freezing-related latent
534 heat eventually cause updrafts to be stronger in the polluted-scenario run starting at ~21:00
535 GMT (Figure 10). Then, the stronger updrafts induce deposition to be greater in the
536 polluted-scenario run around 21:10 GMT (Figure 10). Note that deposition-related latent
537 heat is about one order of magnitude greater than freezing-related latent heat for a unit
538 mass of hydrometeors involved in phase-transition processes. This contributes to much
539 greater differences in deposition-related latent heat during period 3 than those in freezing-
540 related latent heat between the runs during period 2 or 3 (Figures 9a and 9b).

541 To satisfy mass conservation, the freezing- and deposition-enhanced updrafts above
542 the freezing level induce more updraft mass fluxes below the freezing level in the polluted-

543 scenario run than in the clean-scenario run for each fire intensity. This leads to more
544 convergence around and below cloud base in the polluted-scenario run. The higher mass
545 fluxes and convergence below the freezing level, in turn, increase condensation starting
546 around 22:30 GMT in the polluted-scenario run (Figure 10). This induces the greater
547 average condensation and condensation-related latent heat in the polluted-scenario run
548 during period 4 (Figure 9c). Enhanced condensation in turn enhances updrafts, establishing
549 a positive feedback between freezing, deposition, condensation, and updrafts, thus further
550 enhancing freezing, deposition, condensation, and updrafts. This enhancement, due to the
551 feedback, eventually determines the overall differences in the pyroCb properties and their
552 impacts on the UTLS water vapor and cloud ice between the runs.

553 Due to the increasing differences in freezing-related latent heat between the polluted-
554 scenario and clean-scenario runs with weakening fire intensity during period 2, those
555 differences in the average freezing-affected updrafts and subsequently in deposition-
556 related latent heat over period 3 increase with weakening fire intensity (Figures 9a, 9b and
557 10). Those differences, calculated using Equation (1), in deposition-related latent heat are
558 16%, 181%, and 417 % for strong, medium, and weak fire intensities, respectively (Figures
559 9b and 10). Since percentage increases in deposition-related latent heat increase, the
560 subsequent percentage increases in updrafts in the polluted-scenario run increase with
561 weakening fire intensity, particularly during period 3 (Figure 10). During period 4, due to
562 these greater increases in updrafts in the polluted-scenario run with weaker fire intensity,
563 the percentage increases in condensation in the polluted-scenario run increase with
564 weakening fire intensity (Figures 9c and 10). The greater increases in condensation cause
565 the greater further enhancement of the increases in updrafts in the polluted-scenario run
566 with weaker fire intensity. This leads to the overall greater effects of fire-produced aerosols
567 on the UTLS water vapor and ice with weaker fire intensity.

568 This section shows that the smaller R_v leads to lower autoconversion rates and a
569 larger amount of cloud liquid as a source of freezing, which in turn induces higher freezing
570 rates and stronger feedbacks between freezing, deposition, condensation and updrafts in
571 the polluted-scenario run than in the clean-scenario run for each fire intensity. This results
572 in stronger updrafts and their impacts on the UTLS water vapor and ice in the polluted-
573 scenario run. The greater R_v reduction among the polluted-scenario runs than among the

574 clean-scenario runs with weakening fire intensity increases the differences in
575 autoconversion, freezing and the feedbacks between the polluted-scenario and clean-
576 scenario runs as fire intensity weakens. This results in the greater impacts of aerosol-
577 induced stronger updrafts on the UTLS water vapor and ice with weaker fire intensity.

578

579 **4.3 Dependence of aerosol effects on the magnitude of aerosol perturbation**

580

581 Table 3 shows that for each of the strong-, medium-, and weak-fire cases, there are
582 increases in the UTLS water-vapor and cirrus-cloud mass in the run with fire-induced
583 aerosol perturbations of 30000 or 7500 cm^{-3} . These increases are relative to the mass in the
584 low-aerosol run for the strong-fire case, in the medium-low run for the medium-fire case,
585 and in the weak-low run for the weak-fire case. Note that for each of the three types of fire-
586 induced aerosol perturbations of 30000, 15000 and 7500 cm^{-3} , aerosol-perturbation-
587 induced percentage increases in the UTLS water-vapor and cirrus-cloud mass increase as
588 fire intensity weakens (Tables 2 and 3). The qualitative nature of results regarding the
589 dependence of the percentage increases in the UTLS water-vapor and cirrus-cloud mass on
590 fire intensity thus does not depend on the magnitude of the fire-induced aerosol
591 perturbation.

592 Until now, we have taken interest in the sensitivity to fire intensity of an aerosol
593 perturbation on pyroCb development, the UTLS water vapor and cirrus clouds. To isolate
594 the sensitivity, we have shown comparisons among sensitivity simulations by varying only
595 fire intensity while maintaining a constant aerosol perturbation. While working well for
596 the isolation aspect, this strategy does not reflect reality well. It may be that weaker fire
597 intensity produces a lower aerosol concentration. This possibility is not that unrealistic,
598 since stronger fires likely involve more material burnt and higher aerosol emissions.

599 With this in mind, we make comparisons among three pairs of simulations: the low-
600 aerosol and control-30000 runs for strong fire vs. the medium-low and medium runs for
601 medium fire vs. the weak-low and weak-7500 runs for weak fire. Among these three pairs,
602 the magnitude of the fire-induced aerosol perturbation decreases with weakening fire,
603 emulating the possibility that weaker fire intensity involves a lower amount of aerosols.
604 The perturbation-related aerosol concentration is 30000 cm^{-3} for strong fire, 15000 cm^{-3} for

605 medium fire, and 7500 cm^{-3} for weak fire. Comparisons among these three pairs show that
606 relative importance of aerosol effects on pyroCb development and its impacts on the UTLS
607 water vapor and cirrus clouds increases for weaker fires, and that it does not matter if the
608 aerosol perturbation decreases or stays constant with weakening fire intensity (Tables 2
609 and 3). In these comparisons, it is also possible that when the fire-induced aerosol
610 perturbation is very low for medium or weak fire intensity, the latent heat perturbation by
611 aerosol perturbation can be very low. This very low latent heat is not large enough to
612 increase the relative importance of those aerosol effects with weakening fire intensity.
613 Based on this, the medium run is repeated with a fire-induced aerosol perturbation of 2000
614 cm^{-3} down from 15000 cm^{-3} (the medium-2000 run). The weak run is repeated with a fire-
615 induced aerosol perturbation of 1000 cm^{-3} down from 7500 cm^{-3} (the weak-1000 run). The
616 percentage increases in the UTLS water-vapor and cirrus-cloud mass from the medium-
617 low to medium-2000 runs or from the weak-low to weak-1000 runs are smaller than the
618 increases from the low-aerosol to control-30000 runs for the case of strong fire. This
619 indicates that when the fire-induced aerosol perturbation decreases too much with
620 weakening fire intensity, the relative importance of aerosol effects on pyroCb development
621 and its impacts on the UTLS water vapor and cirrus clouds no longer increases with
622 weakening fire intensity.

623 Results in this section show that the increasing impacts of the fire-induced aerosol
624 perturbations on the UTLS water vapor and cirrus clouds with weakening fire intensity are
625 robust whether or not aerosol perturbations vary with fire intensity unless their variation is
626 extremely high.

627

628 **5. Conclusions**

629

630 This study investigates an observed case of a pyroCb using a modeling framework. In
631 particular, this study focuses on effects of fire-produced aerosols on pyroCb development
632 and its impacts on the UTLS water vapor and cirrus clouds. Results show that the pyroCb
633 efficiently transports water vapor to the tropopause and above. This leads to a much greater
634 amount of water vapor around and above the tropopause (i.e., the UTLS) over the pyroCb
635 compared to that outside the pyroCb. The pyroCb also generates a deck of cirrus clouds

636 around the tropopause. The role of fire-produced aerosols or the fire-induced aerosol
637 perturbation in the water-vapor transport to the UTLS and the production of cirrus clouds
638 becomes significant as fire intensity weakens.

639 During the initial stage, there is a similar LWC between the polluted-scenario and
640 clean-scenario runs for each fire intensity. The reduction in LWC with weakening fire
641 intensity among the polluted-scenario runs is similar to that among the clean-scenario runs.
642 Much greater N_d is in the polluted-scenario run than in the clean-scenario run for each fire
643 intensity. N_d decreases are smaller among the polluted-scenario runs than among the clean-
644 scenario runs with weakening fire intensity. This situation during the initial stage induces
645 R_v to decrease much more among the polluted-scenario runs with weakening fire intensity.
646 This reduces autoconversion more among the polluted-scenario runs and increases
647 differences in autoconversion between the polluted-scenario and clean-scenario runs as fire
648 intensity weakens. The increasing differences in autoconversion between the runs cause
649 greater differences in freezing-related latent heat as fire intensity weakens. Through
650 feedback between freezing, deposition, updrafts, and condensation, differences in freezing-
651 related latent heat induce those in updrafts between the runs. Those greater differences in
652 freezing-related latent heat lead to greater differences in updrafts, producing the greater
653 differences in the UTLS water vapor and cirrus clouds between the runs with weaker fire
654 intensity. This means that the role of fire-produced aerosols in the water-vapor transport to
655 the UTLS and the production of cirrus clouds becomes more significant as fire intensity
656 weakens. This more significant role of fire-produced aerosols with weaker fire intensity is
657 robust to the magnitude of a given fire-induced aerosol perturbation, and the variation of
658 the fire-induced aerosol perturbation with fire intensity unless the variation is very high.

659 The level of understanding of the role played by fire-produced aerosols in the
660 development of pyroCbs and their impacts on the UTLS water vapor and cirrus clouds has
661 been low. This study shows that fire-produced aerosols can invigorate updrafts and
662 convection and thus enhance the transport of water vapor to the UTLS and the formation
663 of cirrus clouds. We find that the mechanism that controls the invigoration of convection
664 by aerosols in the pyroCb is consistent with the traditional invigoration mechanism
665 proposed and described by Koren et al. (2008) and Rosenfeld et al. (2008). However, this
666 study shows that for pyroCbs produced by strong fires, the aerosol-induced invigoration

667 and its effects on the UTLS water vapor and cirrus clouds are insignificant. Note that
668 traditional understanding generally focuses on effects of fire-produced heat and water
669 vapor and their associated surface fluxes on the pyroCb and does not consider effects of
670 fire-produced aerosols on the pyroCb. This understanding adequately explains the
671 mechanics for pyroCbs in association with strong fires. This study suggests that when
672 pyroCbs form over weak-intensity fires, those effects of fire-produced aerosols require
673 consideration.

674 Note that when fire-induced aerosol perturbations are strongly reduced for cases of
675 weaker-intensity fires compared with strong-intensity fires, the significance of the role of
676 the fire-produced aerosol perturbation no longer increases and starts to decrease with
677 weakening fire. This suggests that there may be a critical level of aerosol perturbation
678 below which the increase in this significance with weakening fire intensity ceases.

679

680

681

682

683

684

685

686

687

688

689

690

691

692

693

694

695

696

697

698 **Author contributions**

699

700 SSL generated the research ideas and goals, performed the simulations, and wrote the
701 manuscript. GK and ZL selected the case, analyzed observations, and provided data to set
702 up the simulations while reviewing and providing comments on the manuscript. CHJ, YSC,
703 JU and WJC revised the manuscript based on the reviewers' comments and performed
704 associated analyses of simulation and observation data.

705

706

707

708

709

710

711

712

713

714

715

716

717

718

719

720

721

722

723

724

725

726

727

728

729 Acknowledgements

730 This study was supported by the National Aeronautics and Space Administration through
731 grant NNX16AN61G and the National Science Foundation through grant AGS 1837811.
732 This study was also supported by the National Strategic Project-Fine particle of the
733 National Research Foundation of Korea (NRF) funded by the Ministry of Science and ICT
734 (MSIT), the Ministry of Environment (ME), the Ministry of Health and Welfare (MOHW)
735 (NRF-2017M3D8A1092022) and the Ministry of Education (NRF-
736 2018R1D1A1A09083227). Additional support was provided by the National Institute of
737 Environmental Research (NIER) funded by the Ministry of Environment (MOE) (NIER-
738 2019-01-02-085).

739

740

741

742

743

744

745

746

747

748

749

750

751

752

753

754

755

756

757

758

759

760 **References**

761

762 Albrecht, B. A.: Aerosols, cloud microphysics, and fractional cloudiness, *Science*, 245,
763 1227–1230, 1989.

764 Andreae, M. O., Rosenfeld, D., Artaxo, P., Costa, A. A., Frank, G. P., Longo, K. M., and
765 Silva-Dias, M. A. F.: Smoking rain clouds over the Amazon, *Science*, 303, 1337–1342,
766 2004.

767 Emanuel, K.: *Atmospheric convection*, Oxford University Press, 580 pp, 1994.

768 Fan, J., Leung, L. R., DeMott, P. J., Comstock, J. M., Singh, B., Rosenfeld, D., Tomlinson,
769 J. M., White, A., Prather, K. A., Minnis, P., Ayers, J. K., and Min, Q.: Aerosol impacts
770 on California winter clouds and precipitation during CalWater 2011: local pollution
771 versus long-range transported dust, *Atmos. Chem. Phys.*, 14, 81–101,
772 <https://doi.org/10.5194/acp-14-81-2014>, 2014.

773 Fan, J., Leung, L. R., Rosenfeld, D., and DeMott, P. J.: Effects of cloud condensation nuclei
774 and ice nucleating particles on precipitation processes and supercooled liquid in
775 mixed-phase orographic clouds, *Atmos. Chem. Phys.*, 17, 1017–1035,
776 <https://doi.org/10.5194/acp-17-1017-2017>, 2017.

777 Fouquart, Y., and Bonnel, B.: Computation of solar heating of the Earth's atmosphere: a
778 new parameterization, *Beitr. Phys. Atmos.*, 53, 35–62, 1980.

779 Fromm, M., Lindsey, D. T., Servranckx, R., Yue, G., Trickl, T., Sica, R., Doucet, P., Godin-
780 Beekmann, S., et al.: The untold story of pyrocumulonimbus, *B. Am. Meteorol. Soc.*,
781 91, 1193, doi:10.1175/2010BAMS3004.1, 2010.

782 Grabowski, W. W., Wu, X., and Moncrieff, M. W.: Cloud resolving modeling of tropical
783 cloud systems during phase III of GATE. Part I: Two-dimensional experiments, *J.*
784 *Atmos. Sci.*, 53, 3684–3709, 1996.

785 Houze, R. A.: *Cloud Dynamics*, Academic Press, 573 pp, 1993.

786 Kablick, G., Fromm, M., Miller, S., Partain, P., Peterson, D., Lee, S. S., Zhang, Y., Lambert,
787 A., and Li, Z.: The Great Slave Lake pyroCb of 5 August 2014: observations,
788 simulations, comparisons with regular convection, and impact on UTLS water vapor,
789 *J. Geophys. Res.*, 123, 12332–12352, <https://doi.org/10.1029/2018JD028965>, 2018.

790 Khain, A.: Notes on state-of-the-art investigations of aerosol effects on precipitation: a

- 791 critical review, *Environ. Res. Lett.*, 4, doi:10.1088/1748-9326/4/1/015004,
792 2009. Khain, A., BenMoshe, N., and Pokrovsky, A.: Factors determining the impact of
793 aerosols on surface precipitation from clouds: Attempt of classification, *J. Atmos. Sci.*,
794 65, 1721–1748, 2008.
- 795 Khairoutdinov, M., and Kogan, Y.: A new cloud physics parameterization in a large-eddy
796 simulation model of marine stratocumulus, *Mon. Wea. Rev.*, 128, 229–243, 2000.
- 797 Knobelspiesse, K., Cairus, B., Ottaviani, M., et al.: Combined retrievals of boreal forest
798 fire aerosol properties with a polarimeter and lidar, *Atmos. Chem. Phys.*, 11, 7045–
799 7067, 2011.
- 800 Koop, T., Luo, B. P., Tsias, A. and Peter, T.: Water activity as the determinant for
801 homogeneous ice nucleation in aqueous solutions, *Nature*, 406, 611–614, 2000.
- 802 Koren I., Martins, J. V., Remer, L. A., and Afargan, H.: Smoke invigoration versus
803 inhibition of clouds over the Amazon, *Science*, 321, 946–949, 2008.
- 804 Koren, I., Altaratz, O., Remer, L. A., et al.: Aerosol-induced intensification of rain from the
805 tropics to the mid-latitudes, *Nat. Geosci.*, 5, 118–122, 2012.
- 806 Krueger, S. K., Cederwall, R. T., Xie, S. C., and Yio, J. J.: GCSS Working Group 4 Model
807 Intercomparison-procedures for Case 3: Summer 1997 ARM SCM IOP. Draft
808 manuscript obtainable from <http://www.arm.gov/docs/scm/scmic3>, 1999.
- 809 Lebo, Z. J. and Morrison, H.: Effects of horizontal and vertical grid spacing on mixing in
810 simulated squall lines and implications for convective strength and structure, *Mon.*
811 *Weather. Rev.*, 143, 4355–4375, 2014.
- 812 Lee, H., and Baik, J.-J.: A physically based autoconversion parameterization, *J. Atmos. Sci.*,
813 74, 1599–1615, 2017.
- 814 Lee, S. S., Kim, B.-G., Nam, H.-G., et al.: Factors that control heavy snowfalls in the
815 eastern coast of Korea, *Terr. Atmos. Ocean. Sci.*, 29, 301-304, 2018.
- 816 Lee, S. S., and Penner, J. E.: Comparison of a global-climate model to a cloud-system
817 resolving model for the long-term response of thin stratocumulus clouds to
818 preindustrial and present-day aerosol conditions, *Atmos. Chem. Phys.*, 10, 6371–6389,
819 2010.
- 820 Lee, S. S., Donner, L. J., Phillips, V. T. J., and Ming, Y.: The dependence of aerosol effects
821 on clouds and precipitation on cloud-system organization, shear and stability, *J.*

- 822 Geophys. Res., 113, D16202, 2008.
- 823 Lee, S. S., Penner, J. E., and Saleeby, S. M.: Aerosol effects on liquid-water path of thin
824 stratocumulus clouds., J. Geophys. Res., 114, D07204, 2009.
- 825 Lee, S. S., Feingold, G., Koren, I., Yu, H., Yamaguchi, T., and McComiskey, A.: Effect of
826 gradients in biomass burning aerosol on circulations and clouds, J. Geophys. Res.,
827 119, 9948–9964, 2014.
- 828 Lee, S. S., Kim, B. -G., Yum, S. S., et al.: Effect of aerosol on evaporation, freezing and
829 precipitation in a multiple cloud system, Clim. Dyn., 48, 1069–1087, 2016.
- 830 Lee, S. S., Li, Z., and Mok, J., et al.: Interactions between aerosol absorption,
831 thermodynamics, dynamics, and microphysics and their impacts on clouds and
832 precipitation in a multiple-cloud system, Clim. Dyn., 49, 3905–3921, 2017.
- 833 Liu, Y., and Daum, P. H.: Parameterization of the autoconversion process. Part I: Analytical
834 formulation of the Kessler-type parameterizations, J. Atmos. Sci., 61, 1539–1548,
835 2004.
- 836 Lohmann, U. and Diehl, K.: Sensitivity studies of the importance of dust ice nuclei for the
837 indirect aerosol effect on stratiform mixed-phase clouds, J. Atmos. Sci., 63, 968–982,
838 2006.
- 839 Luderer, G., Trentmann, J., Winterrath, T., Textor, C., Herzog, M., Graf, H., and Andreae,
840 M.: Modeling of biomass smoke injection into the lower stratosphere by a large forest
841 fire (part ii): Sensitivity studies. Atmos. Chem. Phys., 6, 5261–5277, 2006.
- 842 Luderer, G., Trentmann, J., and Andreae, M.: A new look at the role of fire-released
843 moisture on the dynamics of atmospheric pyro-convection, Int. J. Wildland Fire, 18,
844 554–562, 2009.
- 845 Mlawer, E. J., Taubman, S. J., Brown, P. D., Iacono, M. J., and Clough, S. A.: RRTM, a
846 validated correlated-k model for the longwave, J. Geophys. Res., 102, 1663–1668,
847 1997.
- 848 Möhler, O., et al.: Efficiency of the deposition mode ice nucleation on mineral dust particles,
849 Atmos. Chem. Phys., 6, 3007–3021, 2006.
- 850 Morrison, H., and Grabowski, W. W.: Cloud-system resolving model simulations of aerosol
851 indirect effects on tropical deep convection and its thermodynamic environment,
852 Atmos. Chem. Phys., 11, 10503–10523, 2011.

- 853 Peterson, D., Fromm, M., Solbrig, J., Hyer, E., Surratt, M., and Campbell, J.: Detection
854 and inventory of intense pyroconvection in western North America using GOES-15
855 daytime infrared data, *J. Appl. Meteorol. Clim.*, 56, 471–493, 2017.
- 856 Phillips, V. T. J., Donner, L. J., and Garner, S.: Nucleation processes in deep convection
857 simulated by a cloud-system-resolving model with double-moment bulk microphysics,
858 *J. Atmos. Sci.*, 64, 738–761, 2007.
- 859 Pruppacher, H. R., and Klett, J. D.: *Microphysics of clouds and precipitation*, 714 pp,
860 Reidel D., 1978.
- 861 Pumphrey, H., Santee, M., Livesey, N., Schwartz, M., and Read, W.: Microwave Limb
862 Sounder observations of biomass-burning products from the Australian bush fires of
863 February 2009, *Atmos. Chem. Phys.*, 11, 6285–6296, 2011.
- 864 Reid, J. S., Hobbs, P. V., Rangno, A. L., and Hegg, D. A.: Relationships between cloud
865 droplet effective radius, liquid water content, and droplet concentration for warm
866 clouds in Brazil embedded in biomass smoke, *J. Geophys. Res.*, 104, 6145–6153,
867 1999.
- 868 Reid, J. S., Koppmann, R., Eck T. F., and Eleuterio, D.: A review of biomass burning
869 emissions part II: intensive physical properties of biomass burning particles, *Atmos.*
870 *Chem. Phys.*, 5, 799–825, 2005.
- 871 Rogers, R. R., and Yau, M. K.: *A short course in cloud physics*, Pergamon Press, 293 pp,
872 1991.
- 873 Rosenfeld, D., Lohmann, U., Raga, G. B., et al.: Flood or drought: How do aerosols affect
874 precipitation? *Science*, 321, 1309–1313, 2008.
- 875 Seinfeld, J. H. and Pandis, S. N.: *Atmospheric Chemistry and Physics: From Air Pollution*
876 *to Climate Change*, John Wiley & Sons, 1326 pp, 1998.
- 877 Solomon, S., Rosenlof, K. H., Portmann, R. W., Daniel, J. S., Davis, S. M., Sanford, T. J.,
878 and Plattner, G. K.: Contributions of stratospheric water vapor to decadal changes in
879 the rate of global warming, *Science*, 327, 1219–1223, 2010.
- 880 Storer, R. L., van den Heever, S. C., and Stephens, G. L.: Modeling aerosol impacts on
881 convection under differing storm environments, *J. Atmos. Sci.*, 67, 3904–3915, 2010.
- 882 Tao, W.-K., Chen, J.-P., Li, Z., Wang, C., and Zhang, C.: Impact of aerosols on convective
883 clouds and precipitation, *Rev. Geophys.*, 50, RG2001, 2012.

884 Trentmann, J., Luderer, G., Winterrath, T., Fromm, M., Servranckx, R., Textor, C., et al.:
885 Modeling of biomass smoke injection into the lower stratosphere by a large forest fire.
886 Part I: Reference simulation. *Atmos. Chem. Phys.*, 6, 5247–5260, 2006.

887 Twomey, S.: The influence of pollution on the shortwave albedo of clouds, *J. Atmos. Sci.*,
888 34, 1149–1152, 1977.

889 Wang, H., Skamarock, W. C., and Feingold, G.: Evaluation of scalar advection schemes in
890 the Advanced Research WRF model using large-eddy simulations of aerosol-cloud
891 interactions, *Mon. Weather. Rev.*, 137, 2547–2558, 2009.

892 Wang, P.: Is the Transport by deep convective storms the major source of stratospheric
893 water vapor?, 99th Annual Meeting, American Meteorological Society, available at
894 <https://ams.confex.com/ams/2019Annual/webprogram/Paper354897.html>, 2019.

895
896
897
898
899
900
901
902
903
904
905
906
907
908
909
910
911
912
913
914
915
916
917
918
919
920
921
922
923

924 **FIGURE CAPTIONS**

925

926

927 Figure 1. Visible image of the fire, smoke and cirrus cloud in association with the selected
928 pyroCb. This image was taken by the visible infrared imaging radiometer suite onboard the
929 Suomi spacecraft. Bright white represents cirrus (anvil) at the top of the pyroCb, and the
930 red circle marks the fire spot. Dark white represents smoke produced by the fire. Adapted
931 from Kablick et al. (2018).

932

933 Figure 2. The simulated fire spot (red circle) and the field of cloud-ice mass density (cirrus
934 cloud) at the top of the simulated pyroCb when it is about to enter its mature stage.

935

936 Figure 3. The vertical distribution of the radar reflectivity averaged along the Cloudsat path.

937

938 Figure 4. Vertical distributions of the average updraft mass fluxes at all altitudes in cloudy
939 areas (i.e., where the sum of LWC and IWC is non-zero) over the simulation period
940 between 17:00 GMT on August 5th and 12:00 GMT on August 6th.

941

942 Figure 5. Vertical distributions of the average water-vapor mass density at altitudes above
943 13 km and over the simulation period between 17:00 GMT on August 5th and 12:00 GMT
944 on August 6th. Colored lines represent the average values over cloudy grid columns (non-
945 zero sum of LWP and IWP). The black line represents those values over non-cloudy
946 columns (zero sum of LWP and IWP) in the control run.

947

948 Figure 6. Vertical distributions of the average cloud-ice mass density at all altitudes in
949 cloudy areas (non-zero sum of LWC and IWC) over the simulation period between 17:00
950 GMT on August 5th and 12:00 GMT on August 6th.

951

952 Figure 7. Same as Figure 6 but for deposition rate.

953

954 Figure 8. Average N_d , R_v , and LWC at all altitudes in cloudy areas over the period between
955 17:00 and 19:00 GMT on August 5th.

956

957 Figure 9. Average rates of condensation, deposition and cloud-liquid freezing at all
958 altitudes in cloudy areas and over periods (a) 2, (b) 3 and (c) 4. In panel (a), average
959 autoconversion rates are also shown.

960

961 Figure 10. Time series of differences in average values of variables related to aerosol-
962 induced invigoration of convection at all altitudes in cloudy areas between the (a) control
963 and low-aerosol runs for strong fire intensity, (b) medium and medium-low runs for
964 medium fire intensity and (c) weak and weak-low runs for weak fire intensity.

965

966

967

968

969

970

971

972

973

974

975

976

977

978

979

980

981

982

983

984

985

986

Simulations	Surface sensible heat fluxes in the fire spot (W m^{-2})	Surface latent heat fluxes in the fire spot (W m^{-2})	Aerosol concentration in the PBL over the fire spot (cm^{-3})
Control run	15000	1800	15000
Low-aerosol run	15000	1800	150
Control-30000	15000	1800	30000
Control-7500	15000	1800	7500
Medium run	7500	900	15000
Medium-low run	7500	900	150
Medium-30000	7500	900	30000
Medium-7500	7500	900	7500
Medium-2000	7500	900	2000
Weak run	3750	450	15000
Weak-low run	3750	450	150
Weak-30000	3750	450	30000
Weak-7500	3750	450	7500
Weak-1000	3750	450	1000

987

988 Table 1. Summary of simulations

989

990

991

992

993

994

995

996

997

998

999

1000

1001

1002

1003

1004

1005

1006

1007

	Back-ground	Control	Low-aerosol	Difference (%)	Medium	Medium-low	Difference (%)	Weak	Weak-low	Difference (%)
Updraft mass fluxes (kg m ⁻² s ⁻¹)		1.23	1.19	3	0.89	0.70	27	0.42	0.21	100
Water-vapor mass density between 13 and 16 km (10 ⁻³ g m ⁻³)	0.46	2.31	2.26	2	1.61	1.32	22	0.93	0.58	60
Cirrus-cloud mass density between 9 and 13 km (g m ⁻³)		0.024	0.023	4	0.017	0.012	42	0.008	0.004	100

1008

1009 Table 2. Average updraft mass fluxes at all altitudes in cloudy areas, the average water-
1010 vapor mass density over altitudes between 13 and 16 km and over cloudy columns except
1011 for the average background water-vapor mass density which is also over altitudes between
1012 13 and 16 km but over non-cloudy columns, and the average cirrus-cloud mass density
1013 between 9 and 13 km in cloudy areas. 16 km is the altitude to which the non-zero water-
1014 vapor mass density over cloudy columns extends (Figure 5). These average values are
1015 obtained over the simulation period between 17:00 GMT on August 5th and 12:00 GMT on
1016 August 6th. “Difference” is the percentage difference between the polluted-scenario and
1017 clean-scenario runs for each fire intensity ($\frac{\text{Polluted-scenario run minus clean-scenario run}}{\text{Clean-scenario run}} \times$
1018 100 (%)).

1019

1020

1021

1022

1023

1024

1025

	Control-30000	Control-7500	Medium-30000	Medium-7500	Medium-2000	Weak-30000	Weak-7500	Weak-1000
Water vapor mass density between 13 and 16 km (10^{-3} g m ⁻³)	2.38 (5%)	2.28 (0.9%)	1.87 (42%)	1.50 (14%)	1.36 (3%)	1.31 (125%)	0.75 (29%)	0.60 (3%)
Cirrus cloud mass density between 9 and 13 km (g m ⁻³)	0.025 (9%)	0.023 (0.2%)	0.023 (92%)	0.014 (17%)	0.012 (3%)	0.013 (225%)	0.006 (50%)	0.004 (8%)

1026

1027 Table 3. Average water-vapor mass density between 13 and 16 km over cloudy columns
 1028 and the average cirrus-cloud mass density between 9 and 13 km in cloudy areas over the
 1029 simulation period between 17:00 GMT on August 5th and 12:00 GMT on August 6th. The
 1030 numbers in parentheses are the percentage differences:

1031 $\frac{\text{Control-30000 (or control-7500) run minus low-aerosol run}}{\text{Low-aerosol run}} \times 100$ (%) for strong fire intensity,

1032 $\frac{\text{Medium-30000 (or medium-7500 or medium-2000) run minus medium-low run}}{\text{Medium-low run}} \times 100$ (%) for

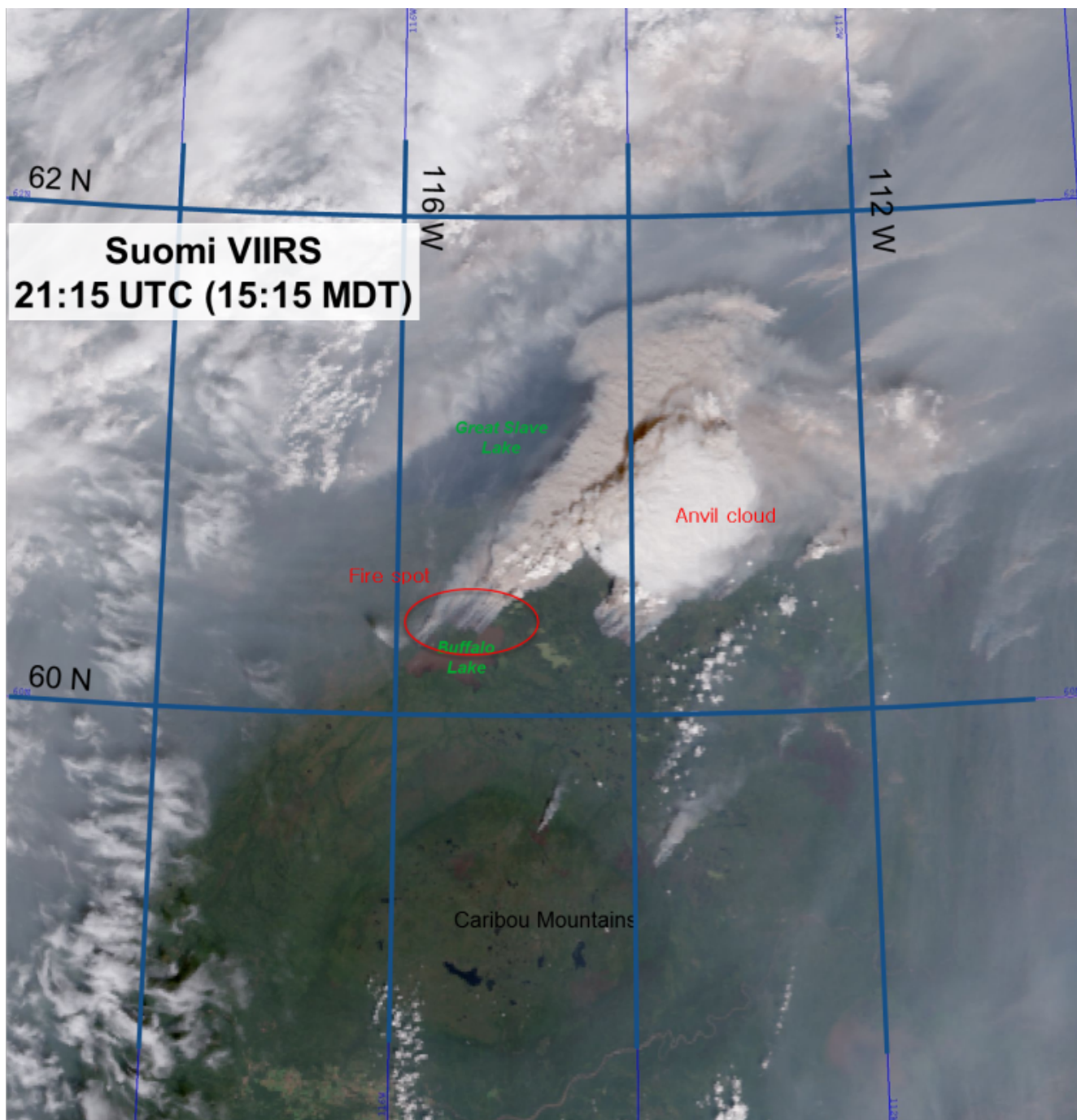
1033 medium fire intensity, and

1034 $\frac{\text{Weak-30000 (or weak-7500 or weak-1000) run minus weak-low run}}{\text{Weak-low run}} \times 100$ (%) for weak fire

1035 intensity.

1036

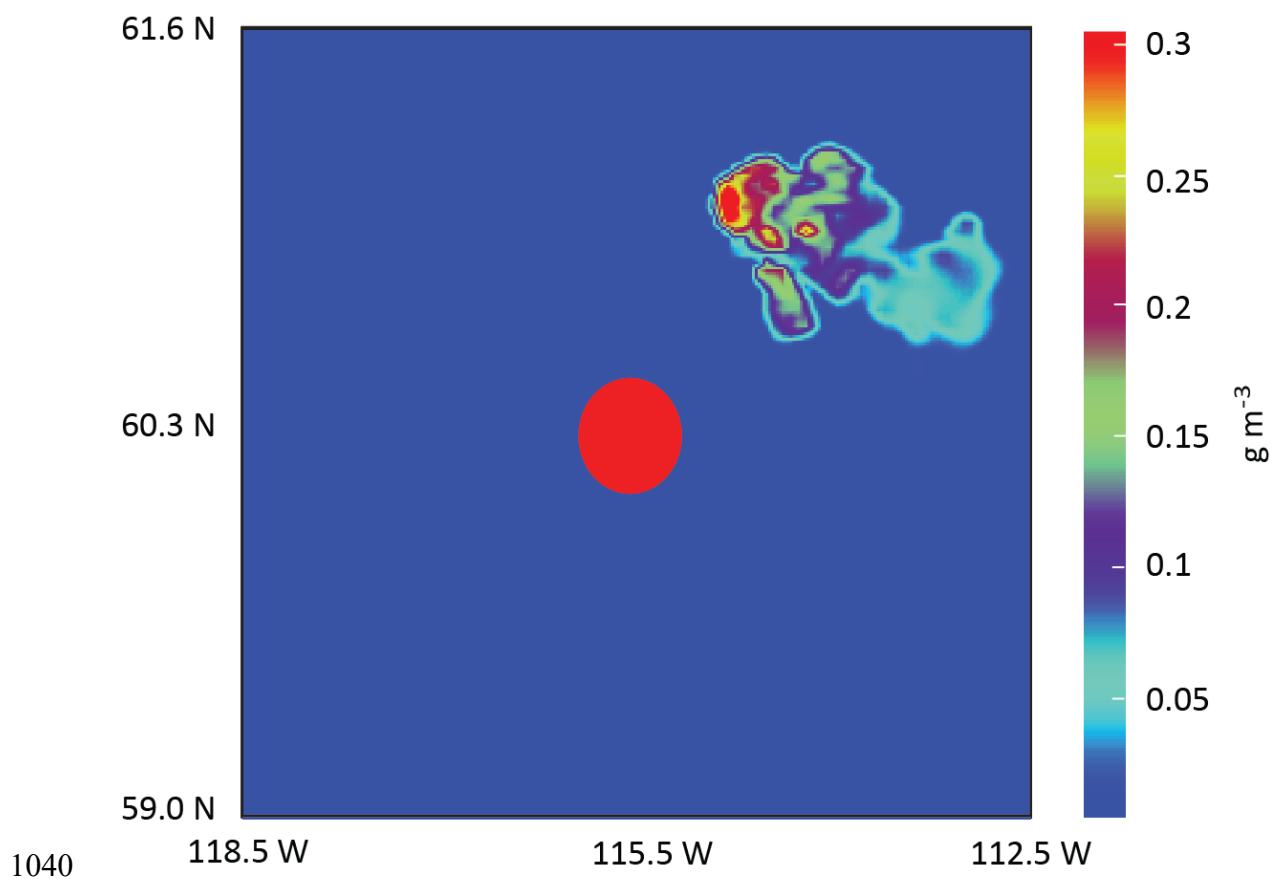
1037



1038

1039

Figure 1



1040

1041

1042

1043

1044

1045

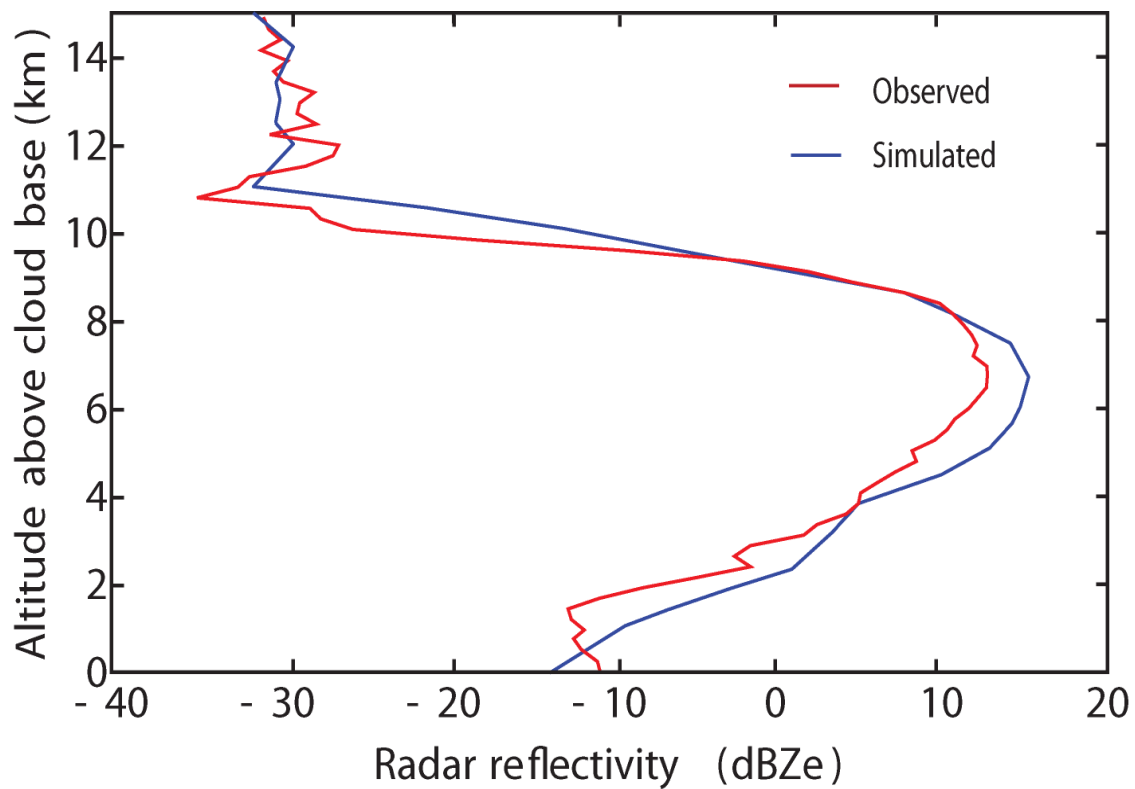
1046

1047

1048

Figure 2

1049



1050

Figure 3

1051

1052

1053

1054

1055

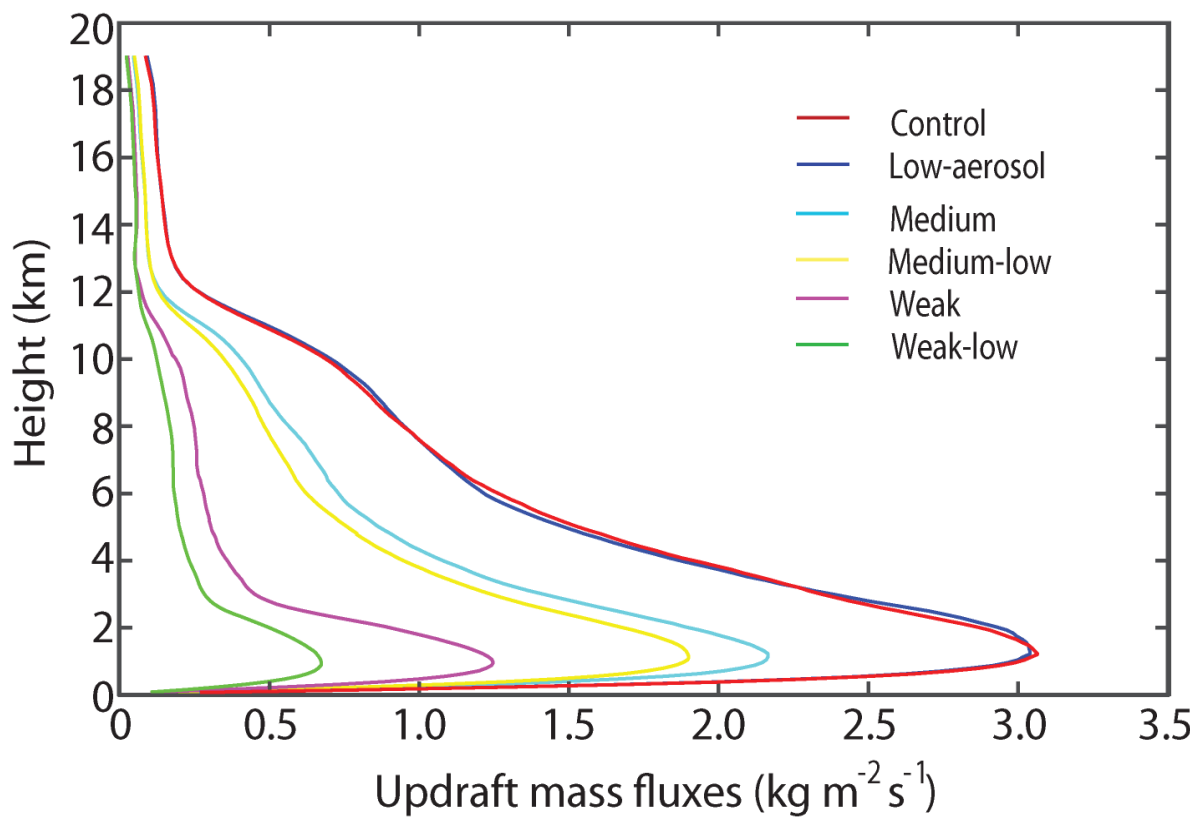
1056

1057

1058

1059

1060



1061

Figure 4

1062

1063

1064

1065

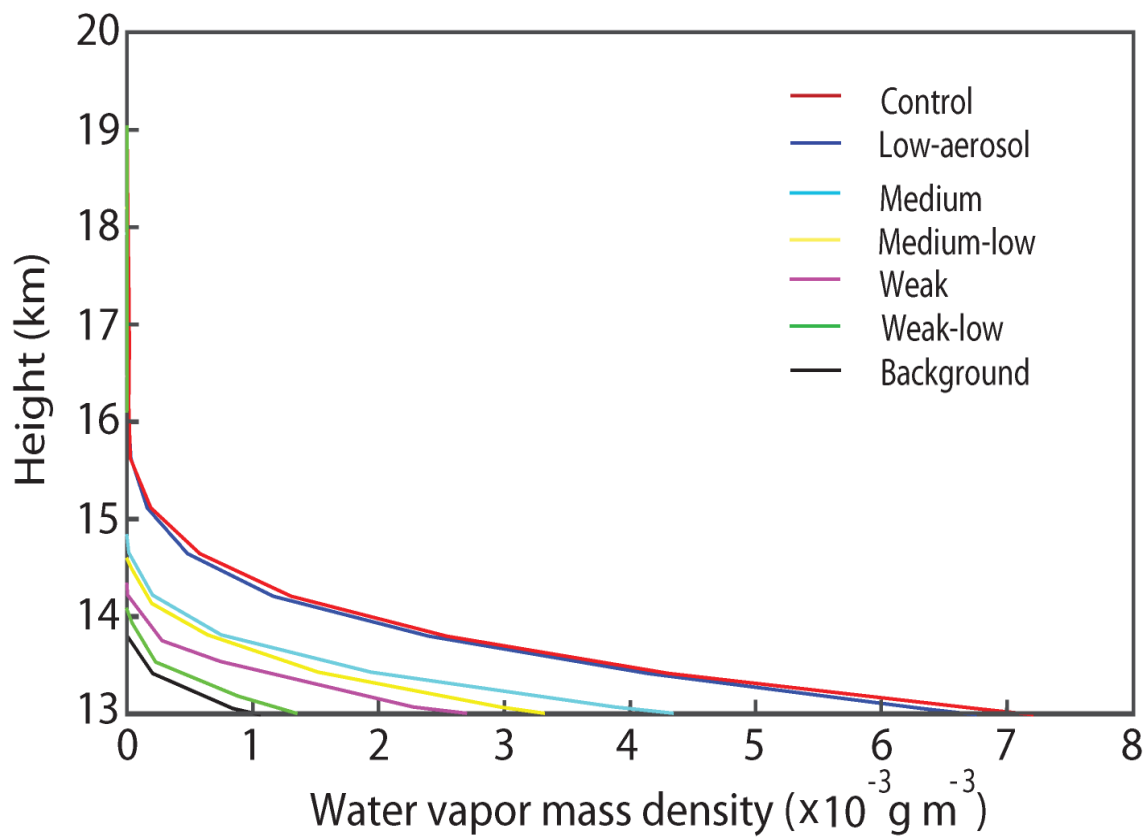
1066

1067

1068

1069

1070



1071

1072

1073

1074

1075

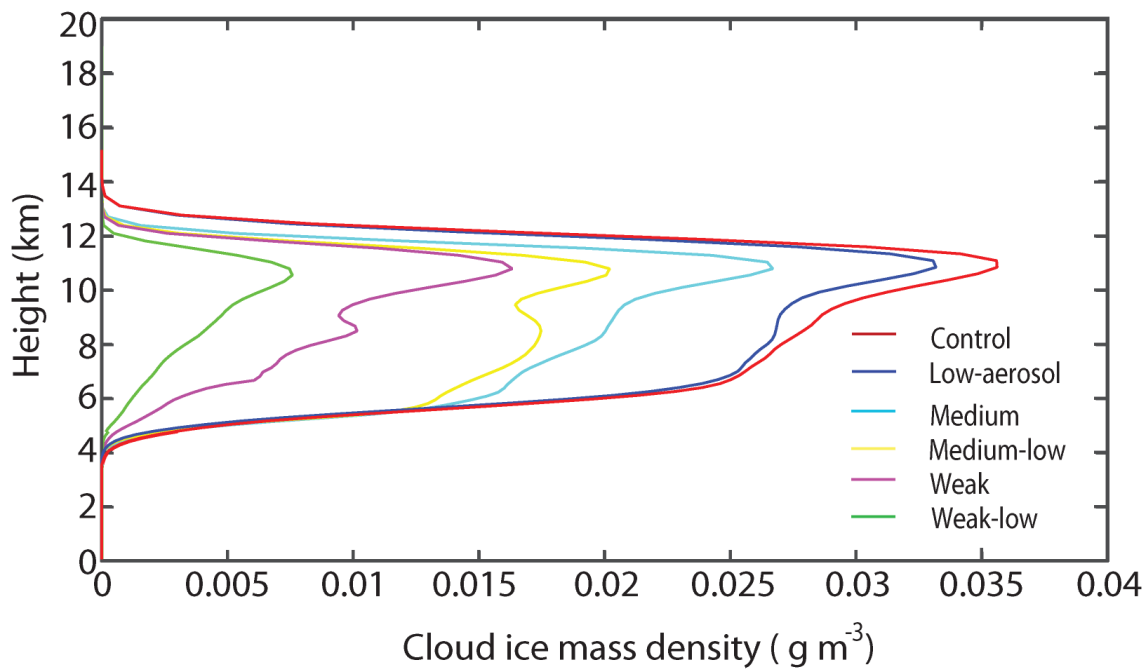
1076

1077

1078

1079

Figure 5



1080

1081

Figure 6

1082

1083

1084

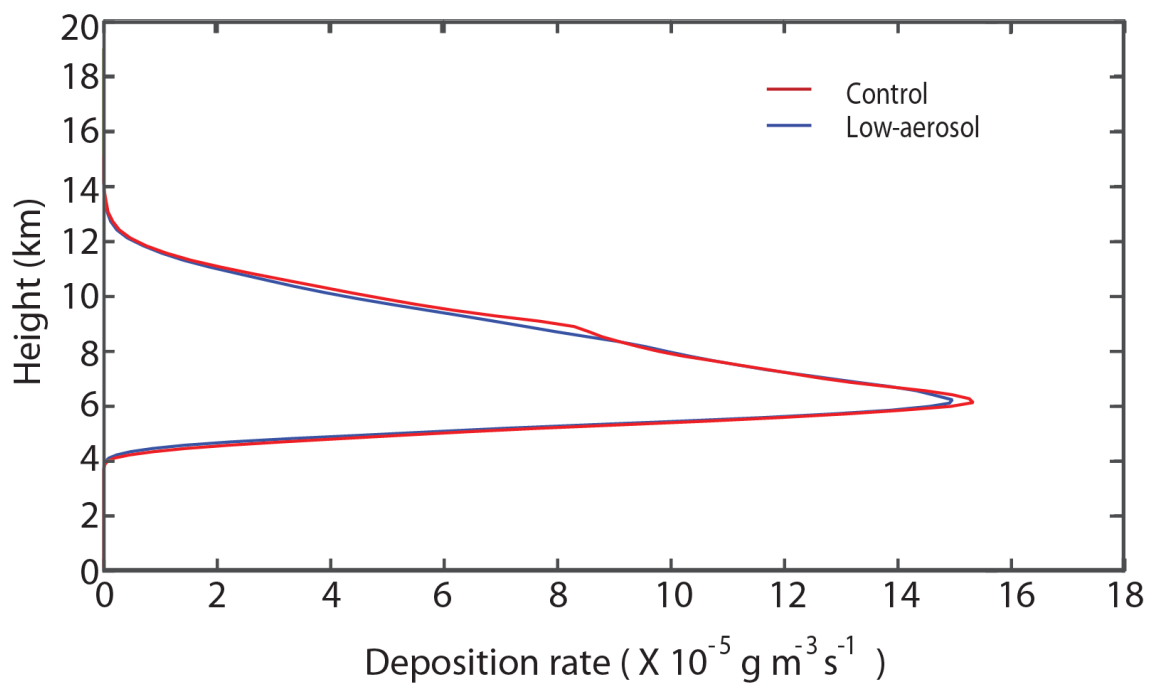
1085

1086

1087

1088

1089



1090

1091

Figure 7

1092

1093

1094

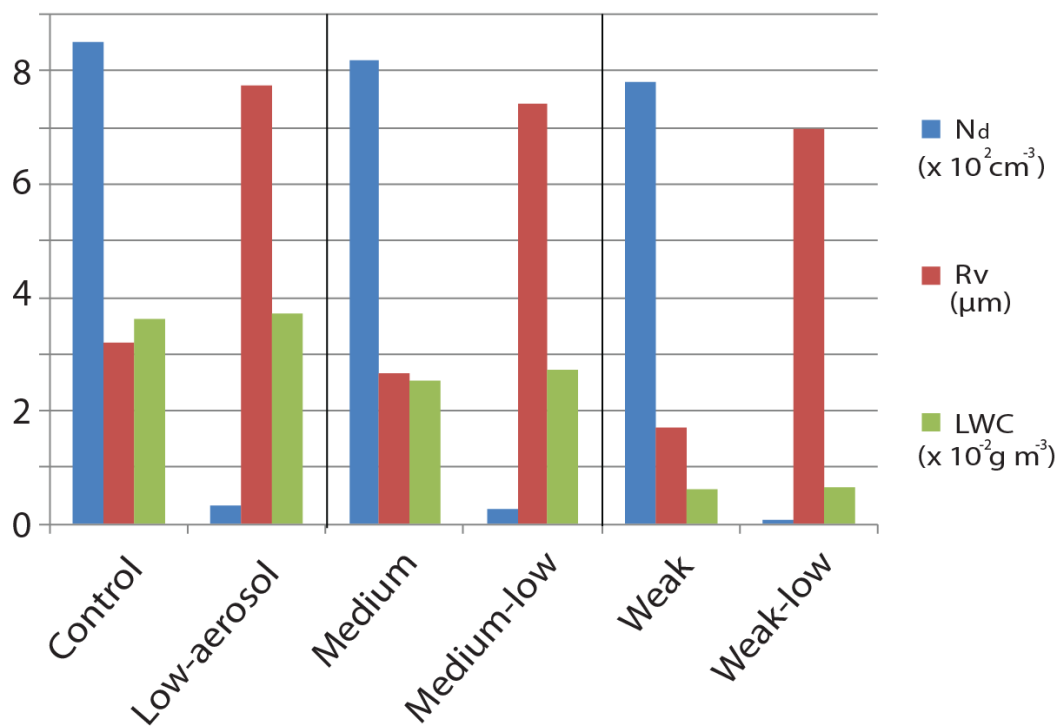
1095

1096

1097

1098

Period 1 (17 GMT - 19 GMT on August 5th; initial stage)



1099

1100

Figure 8

1101

1102

1103

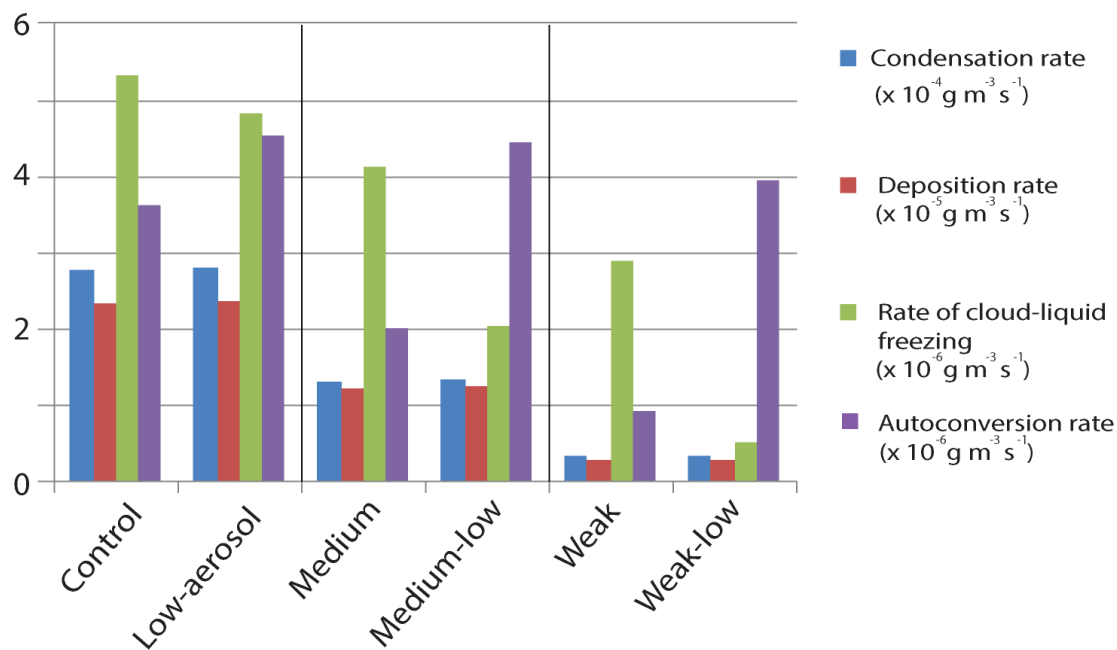
1104

1105

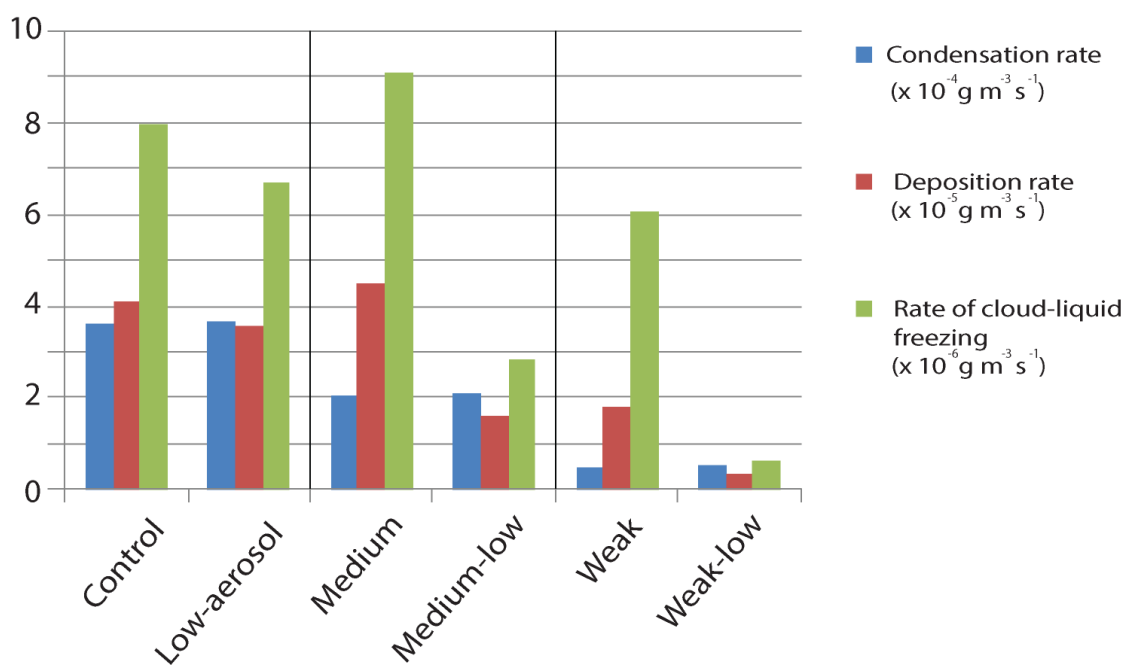
1106

1107

a Period 2 (19 GMT - 21 GMT on August 5th; initial stage)



b Period 3 (21 GMT - 23 GMT on August 5th; initial stage)



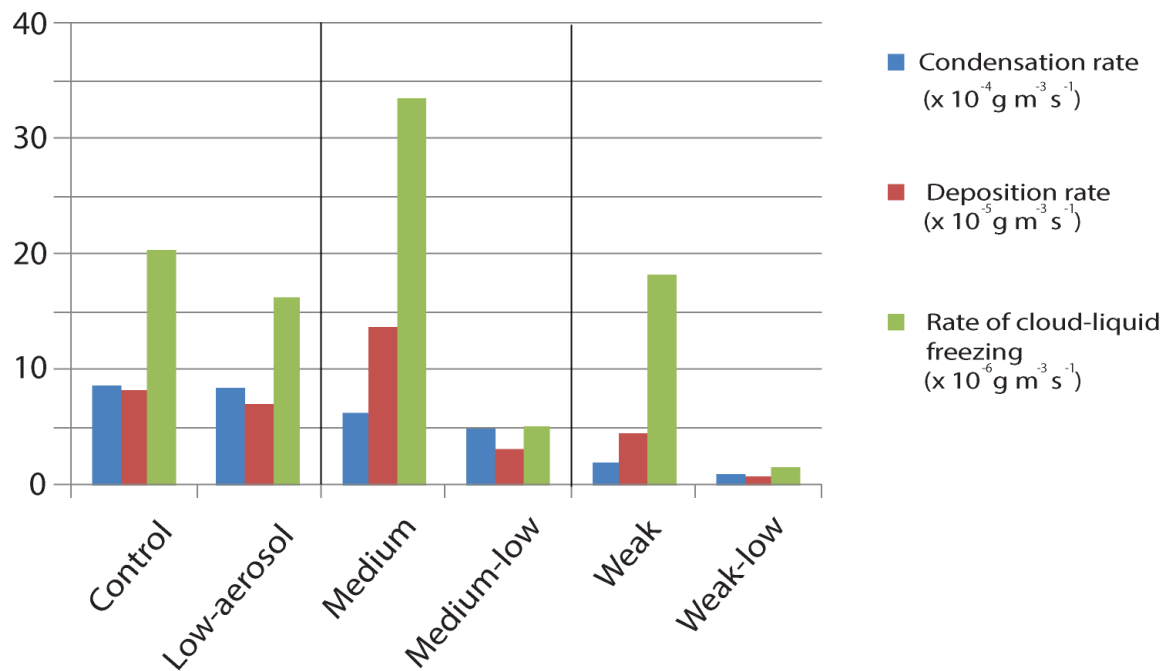
1108

1109

Figure 9

1110

C Period 4 (23 GMT on August 5th - 12 GMT on August 6th
; mature and decaying stages)



1111

1112

Figure 9

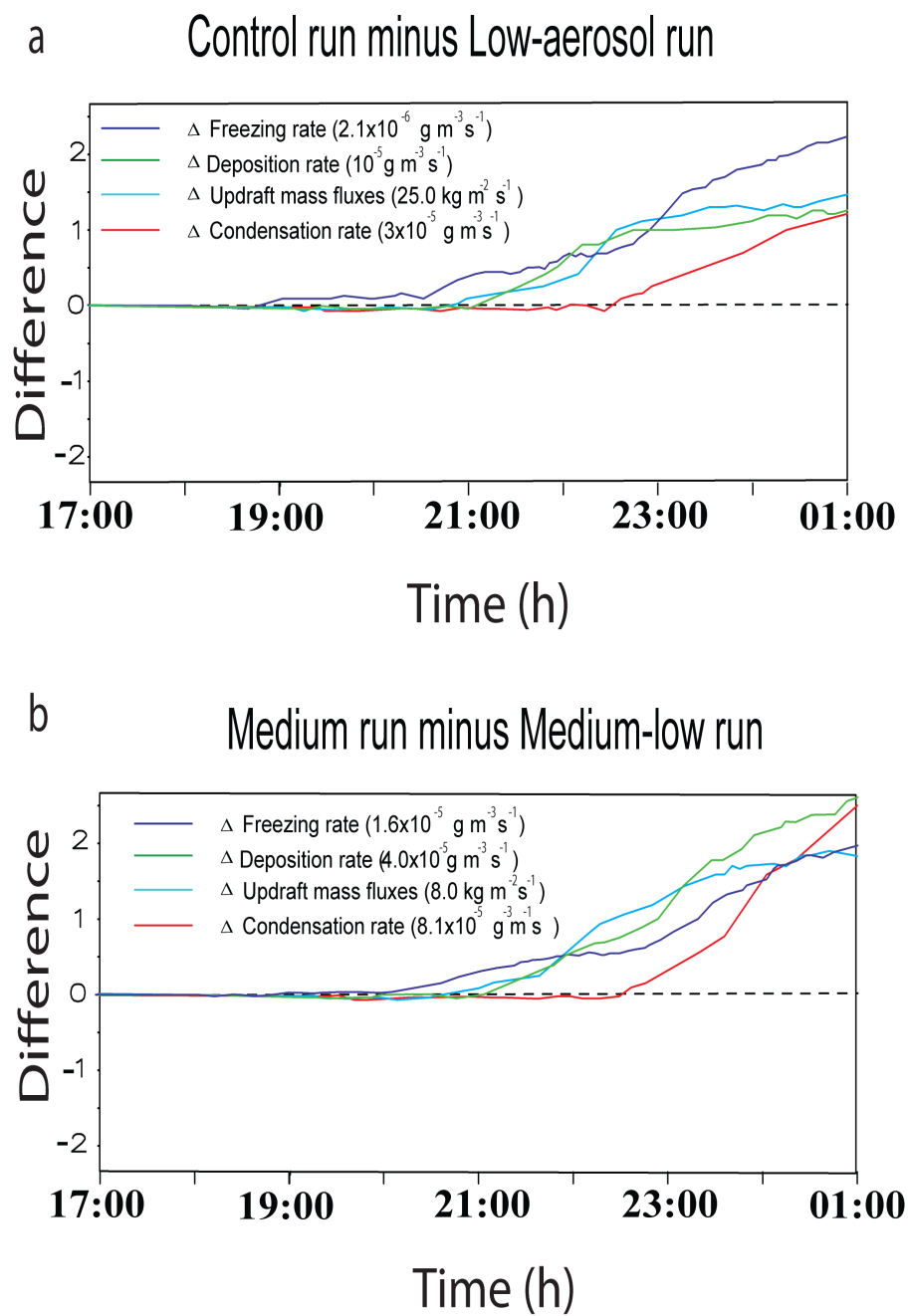
1113

1114

1115

1116

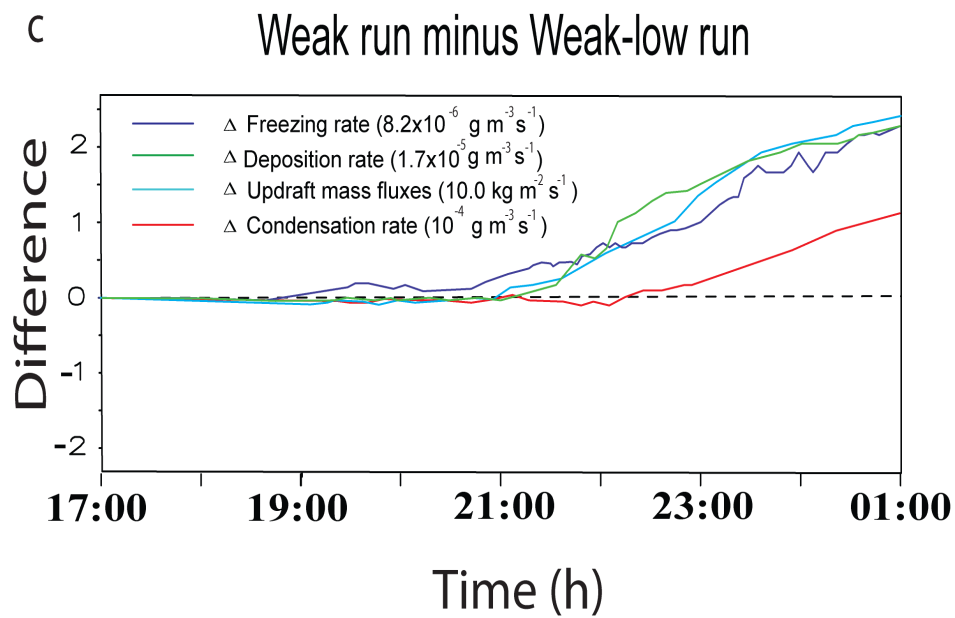
Differences in the averaged values



1117

1118

Figure 10



1119

1120

Figure 10

1121

1122

1123

1124

1125

1126

1127